RICE UNIVERSITY

SEARCH FOR ADDITIONAL GAUGE BOSONS

BY

GEARY W. EPPLEY

A THESIS SUBMITTED
IN PARTIAL FULFILLMENT OF THE
REQUIREMENTS FOR THE DEGREE

DOCTOR OF PHILOSOPHY

APPROVED, THESIS COMMITTEE

Hannu E. Miettinen, Chairman
Professor of Physics

Marjorie D. Corcoran
Professor of Physics

John C. Polking
Professor of Mathematics

HOUSTON, TEXAS

APRIL, 1995

Abstract

Search for Additional Gauge Bosons

by

Geary W. Eppley

We have searched for evidence of $W' \to e\nu$ and $Z' \to ee$ in data collected with the DØ detector at the Tevatron during the 1992–1993 $p\overline{p}$ collider run at $\sqrt{s} = 1.8$ TeV. We set an upper limit at the 95% confidence level on the cross section times branching ratio for $W' \to e\nu$, assuming that the neutrino from W' decay is stable and has a mass significantly less than $m_{W'}$, and an upper limit on $Z' \to ee$. We exclude the existence of a W' of mass less than 610 GeV and a Z' of mass less than 490 GeV at the 95% confidence level, assuming standard model couplings to quarks and leptons.

Acknowledgments

I would like to thank the members DØ Collaboration, in particular those I got to know while getting the detector ready, running shifts, and otherwise working at DØ, for making this an immensely rewarding an enjoyable experience; those who have contributed directly to this analysis by sharing their own analysis, providing essential software, many helpful discussions, or reviewing and editing parts of this analysis: Hiro Aihara, Rich Astur, Jeff Bantly, Jerry Blazey, Andrew Brandt, Brajesh Choudhary, Marcel Demarteau, Sal Fahey, Mirek Fatyga, Eric Flattum, Krzysztof Genser, Norman Graf, Paul Grannis, Peter Grudberg, Uli Heintz, John Jiang, Bob Kehoe, Mike Kelly, Ron Madaras, Wyatt Merritt, Hugh Montgomery, Meena Narain, Adam Para, Srini Rajagopalan, Michael Rijssenbeek, Natalie Roe, John Sculli, Joey Thompson, Mike Tartaglia, Harry Weerts, Darien Wood, Jie Yang, Taka Yasuda, and other members of the W-Z physics analysis group; Dhiman Chakraborty, Serban Protopopescu, and the other members of the top group who were of invaluable help in the PDE top analysis not included in this thesis; Qiang Zhu, who introduced me to the methods of accessing DØ data; Azriel Goldschmidt, whose complementary analysis for right-handed W's has led to many fruitful discussions; Pablo Yepes, my collaborator on the W' analysis; my office mate, Tony Empl, who answered innumerable questions concerning PAW, LATEX, and UNIX; professors Paul Stevenson and Marj Corcoran of Rice University for helpful discussions and editorial guidance; and my advisor, Hannu Miettinen, for his sage advice and wise counsel.

I would like to thank my wife, Felicia, who has made this possible.

Table of Contents

Abstract ii

Acknowledgments iii

Table of Contents iv

List of Figures vi

List of Tables viii

1 Introduction **1**

1.1 Preface 1

1.2 The standard model, a brief history 1

1.3 Models for additional W, Z. 12

1.4 This study 14

2 Experimental apparatus **18**

2.1 The Tevatron 18

2.2 The DØ detector 22

2.2.1 The central detector 23

2.2.2 The calorimeter 28

2.2.3 The muon system 30

2.2.4 The trigger 30

3 W' search **32**

3.1 Data sample 32

3.2 Event selection 32

3.3 Selection efficiency 35

3.3.1 Kinematic and geometric acceptance 35

3.3.2 Trigger efficiency 36

3.3.3 Event reconstruction efficiency 37

3.4 QCD background 41

3.5 W cross section 44

3.6 Comparison of the background model to data 44

3.7 W' Monte Carlo 54

3.8 Extracting a limit 55

4 Z' search **60**

4.1 Data sample 60

4.2 Event selection 60

4.3 QCD background 62

4.4 Comparison of Monte Carlo to data 69

4.5 Z' Monte Carlo 71

4.6 Extracting a limit 73

5 Conclusions **77**

References **78**

List of Figures

2.1 A schematic drawing of the Fermilab collider, not to exact scale. In particular, the Tevatron and the Main Ring both have a radius of 1,000 meters. . . . 20

2.2 A one quarter section schematic of the central tracking system and the calorimeter. The center of the detector is the lower left corner. The angular units are pseudorapidity, η. 24

2.3 A cut away view of the DØ detector. The external rectilinear structure is the toroidal magnets and drift tubes of the muon detection system. The large cylindrical structure is the calorimeter. The innermost cylinder is the central tracking system. 25

2.4 The central tracking system. 27

2.5 A cut away view of the liquid argon calorimeter. 29

3.1 The electron E_T for data (discrete points) and W Monte Carlo plus QCD. . 46

3.2 Electron η for data (discrete points) and W Monte Carlo plus QCD. 47

3.3 The $\not{E}_T$ for data (discrete points) and W Monte Carlo plus QCD. 48

3.4 The E_T of the leading hadronic jet for data (discrete points) and W Monte Carlo plus QCD. 49

3.5 The η of the leading jet for data (discrete points) and W Monte Carlo plus QCD. 50

3.6 The W P_T for data (discrete points) and W Monte Carlo plus QCD. 51

3.7 Electron-neutrino transverse mass distribution for data compared to W Monte Carlo plus QCD background. 53

3.8 95% CL upper limit as a function of $m_{W'}$ for $\sigma B(W' \to e\nu)/\sigma B(W \to e\nu)$. The expected value using standard model coupling is also shown. 59

4.1 The Z–Drell-Yan and QCD backgrounds to Z'. 70

4.2 Observed dielectron events (discrete points) are compared to the combined Z–Drell-Yan and QCD background. 72

4.3 95% CL upper limit as a function of $m_{Z'}$ for $\sigma B(Z' \to ee)/\sigma B(Z \to ee)$. The expected value using standard model coupling is also shown. 76

List of Tables

1.1 The elementary particles 11

3.1 Parameters used in the fast Monte Carlo for calorimeter energy resolution and the angular resolution for electrons. 38

3.2 For each W' mass: W' acceptance relative to W, minimum $m_T^{e\nu}$ of the fit region, the 95% CL expressed as expected events, and the 95% CL expressed as $\sigma B(W' \to e\nu)/\sigma B(W \to e\nu)$. 54

4.1 For each Z' mass: minimum m_{ee} of the fit region, the 95% CL expressed as expected events, and the 95% CL expressed as $\sigma B(Z' \to ee)/\sigma B(Z \to ee)$. . . 75

Chapter 1

Introduction

1.1 Preface

It is the belief of this author that at least some part of a PhD thesis should be accessible to a general university audience. Section 1.2, *The standard model, a brief history,* is intended to fulfil that purpose. The more scientifically literate and interested reader may also find Section 1.3, *Models for additional W and Z,* and Chapter 2, which describes the Tevatron and the DØ experiment, of interest. Unfortunately, in the remaining portions of the thesis, some familiarity with the technical jargon of particle physics is assumed.

1.2 The standard model, a brief history

The standard model is the accepted theory describing elementary particles and their interactions. Current experimental results agree well with all predictions of the standard model. It is nonetheless not considered to be the ultimate or most fundamental theory. What follows is an attempt to give a very brief history of the standard model and to describe the reasons that the theory is thought to be incomplete. It is the lack of belief in the finality of the standard model which motivates the search that is the subject of this thesis.

About 600 B.C. Thales of Miletus proposed that the complex physical world was a manifestation of a single simple substance – water. This is the first known instance in Western culture of the idea that a fundamental and simplifying principle could explain complex phenomena. We do not know first-hand the details of Thales' argument but do

know that it was a reasoned argument.

About 200 years after Thales, Democritus of Abdera proposed that matter is composed of very small indivisible entities – atoms. Aside from the fact that Democritus' idea is essentially correct, it is interesting since Democritus moved to a level of abstraction beyond Thales and proposed a hypothetical entity as a simplifying fundamental principle. This is, of course, not yet science. There is no concept of experimental verification or mathematical prediction. But it is a type of proto-theoretical-physics in the sense that fundamental explanations are sought and the explanations are natural, not supernatural [1].

Observational science, mathematics, and engineering flourished at various times and places in the ancient world, but a sustained tradition of experimental science first developed in Western Europe after the Renaissance. In the early 1600's, Galileo Galilei investigated the motion of projectiles and freely falling objects, recorded his results numerically, and correctly deduced the laws of motion for these objects. Drawing on this and other experimental insights, Isaac Newton, born the year Galileo died, formulated the laws governing the motion of physical objects in terms of the reaction of mass to force. These laws are written in concise mathematical form, calculus, that Newton invented for this purpose. Newton, generalizing from his laws of mechanics and from Galileo's work, was able to postulate a universal law of gravitation. There is only one free parameter in the theory, the gravitational coupling strength, which must be determined by experiment. With Newton, we have a mathematically grounded experimental and theoretical physics. We also have the concept that physical law is universal, that it applies everywhere and at all times [2].

Chemists soon learned that whereas all matter was not made from water, it was made from certain fundamental substances called elements. This discovery greatly simplified

our understanding of matter since there are many orders of magnitude (factors of 10) more substances than there are elements. Since, as it eventually turned out, there are 92 naturally occurring elements, elements did not seem to be the final or fundamental explanation of matter. By the early 1800's, the atomic theory of matter was being developed, culminating in 1869 in Dmitri Mendeléev's arrangement of the elements into the periodic table. Despite atomic theory's great experimental success, there were still a few reputable scientists at the end of the 19th century who accepted it only as a useful mathematical abstraction [3].

About the same time that the evidence for the reality of atoms became overwhelming, it was discovered that atoms were not fundamental. In 1897, J. J. Thomson discovered the electron as a free particle and in 1911, Ernest Rutherford discovered the nucleus of the atom. By the early 1930's, it was determined that the nucleus was composed of protons and neutrons. With this simple model of atomic structure – a nucleus of protons and neutrons surrounded by a cloud of electrons – chemistry is explained and all matter is seen to consist of three fundamental particles: the electron, proton, and neutron.

This picture did not last long. By the early 1960's, particle physicists had discovered hundreds of subatomic particles generically referred to as hadrons. Hadrons could be organized in families with regular properties. This classification, which was a kind of periodic table for subatomic particles, was seen to follow certain patterns which corresponded directly to abstract patterns that had been described and classified in a branch of mathematics called group theory. In particular, these patterns corresponded to the symmetry group $SU(3)$. This led to the postulation of the quark model by Murray Gell-Mann and George Zweig, independently, in 1964. Rutherford had discovered the nucleus of the atom by scattering alpha particles, helium nuclei, off of gold foil. The nucleus was found to be

almost point-like in comparison to the size of an atom. In an analogous way, the results of deep inelastic scattering of electrons by protons reported in 1969 disclosed the existence of point-like entities within the proton. Thus protons, neutrons, and the other hadrons were now seen to be constructed from three types of quarks, the up quark, the down quark, and the strange quark. The strange quark is produced in high energy collisions and is not found in ordinary matter. The proton and neutron are constructed from up and down quarks. Ordinary matter is then composed of three elementary particles, the electron which had remained intact and point-like, the up quark, and the down quark.

We need to discuss forces at this point. There are four fundamental forces: gravitation, electromagnetism, the weak force, and the strong force. Newton's theory of gravitation came first, historically. Newton's gravitation law was replaced by one of more universal form in Albert Einstein's theory of general relativity. Einstein's equation accounts for the affect of gravity by altering the geometry of space-time, but the equation is still simple and there is still the same free parameter, the gravitational coupling strength, to be learned from experiment. Remarkably, Einstein's gravitational field equation also expresses the universal conservation of energy and momentum.

The second force to be theoretically understood was electromagnetism. Electricity and magnetism were discovered to be separate but linked manifestations of the same force in the 1800's. James Maxwell wrote down a set of equations describing this force in 1864. It is a postulate of physics that the laws of physics must be the same in every reference frame. H. Lorenz derived a set of mathematical transformations that are the only transformations under which Maxwell's equations would be invariant in any reference frame. Einstein recognized this and also recognized that the same transformations would be obtained if one

postulated that the speed of light is constant in any reference frame. A precision test of this possibility indicated that the measured speed of light is independent of the motion of the observer. This physical interpretation of the Lorentz transformations is Einstein's theory of special relativity, published in 1905.

Quantum mechanics was invented in 1924-1926 to explain the behavior of elementary particles at the atomic level. Quantum electrodynamics, QED, is an extension of quantum mechanics that is invariant under the transformations of special relativity. QED describes the electromagnetic force at the particle level and was first formulated by Paul Dirac in 1926. QED was further developed by many people over the next 20 years, culminating in the independent development of a renormalizable version of QED by Sin-itiro Tomonaga, Julian Schwinger, and Richard Feynman, first presented in 1947. A renormalizable theory is one in which certain infinities that arise in the theory due to the self-interaction of the electron or interaction of the electron with the vacuum are removed by a special mathematical treatment. Such interactions arise in all quantum field theories and modify somewhat the strength of the forces described. These interactions are called higher order or radiative corrections. Because of its relative ease of computation, it is Feynman's formulation of QED that has survived and become the basis of other quantum field theories.

In classical physics, that is before quantum mechanics, the electromagnetic interaction was characterized by postulating a field surrounding each charged object. Two charged particles interacted by each interacting with the field of the other. In a quantum field theory, the interaction of two particles is described as the exchange of a third particle between them. This exchanged particle carries a quantum of energy representing the strength or force of the interaction. The carrier of the force in QED is the photon. Force carrying particles

are bosons which are treated statistically in quantum mechanics in a way that allows many bosons to have exactly the same energy. It is this property of photons that allows lasers to work. In the mathematical description of QED, each charge carrier, for example an electron, necessarily gets a phase as part of its mathematical description. The phase is not detectable in principle but a choice of phase must be made to make sensible calculations in the theory. If one postulates that the phase can take on arbitrary values at each point, called local invariance, then the theory demands that there exist a force carried by massless bosons, in this case the photon. Through a historical accident, this invariance in the theory due to a local choice of phase is called local gauge invariance. The force carrying particles are called gauge bosons because their existence is demanded by local gauge invariance.

The third force is the weak force. The first experimental evidence of the weak force was the discovery by Henri Becquerel in 1896 that uranium compounds would expose covered photographic plates. He detected what is known as beta decay,

$$n \rightarrow pe\bar{\nu},$$

a neutron n decays to a proton p, electron e, and a neutrino ν. The electron from this process was originally called a beta-ray before it was identified as an electron, hence the term beta decay. The existence of the neutrino was first postulated by Wolfgang Pauli, in 1930, to preserve energy and momentum conservation in this reaction. Neutrinos are neutral (without charge) and massless or nearly so. They interact only through the weak force, hence rarely interact with matter. Neutrinos were first experimentally observed directly in 1956. Neutrinos and electrons are called leptons, light particles. In 1931 Dirac proposed the existence of the positron, a positively charged electron, which is the antiparticle of the

electron. The first experimental evidence of positrons was reported later that same year. It is now an essentially fully verified hypothesis that every type of elementary matter particle has an associated antiparticle. The overline notation, $\bar{\nu}$, indicates an antineutrino.

All particles are either described as fermions or bosons. The elementary matter particles–electrons, neutrinos, and quarks– are described in quantum mechanics as fermions. All particle have an intrinsic property called spin which for elementary fermions may have only two values, +1/2 and -1/2. Fermions also have the interesting property that no two otherwise identical fermions may have exactly the same energy. It is this property of electrons that accounts for the different chemical properties of atoms. Helicity is the spin of the particle with respect to its direction of motion and may be either left-handed or right-handed.

In 1934, Enrico Fermi wrote down an equation for the weak interaction in beta decay by analogy with the known equation for the electromagnetic interaction. As it turned out, there are five possible mathematical forms this interaction might take that are compatible with special relativity. It was determined by a number of experiments, beginning in 1957, that only left-handed electrons and neutrinos or right-handed positrons and antineutrinos participated in the weak interaction. Later in 1957, a number of physicists, independently, correctly surmised that, of the five mathematically permitted forms, nature chose a combination of two, vector minus axial-vector (V-A), for the weak interaction. It is an axiom of modern field theory that forces are transmitted by particles called gauge bosons. The charged carrier of the weak force is the W boson. Beta decay may be represented:

$$n \rightarrow pW^{-} \rightarrow pe\bar{\nu},$$

a neutron changes into a proton by emitting a W which immediately decays into an electron and an antineutrino.

It was speculated that there would also exist a neutral version of the weak force carried by the neutral gauge boson, the Z, but this interaction had not been observed. In 1967, Steven Weinberg and Abdus Salam independently proposed a unified electroweak theory based on the symmetry group $SU(2)_L \times U(1)$. Electromagnetic theory had been successfully renormalized (rid of infinities) because the carrier of the force, the photon, had zero mass. To allow for massive bosons, the W and Z, in a renormalizable theory, a special form of spontaneous symmetry breaking called the Higgs mechanism is employed. Electroweak theory predicts three heavy bosons the W^+, W^-, and the Z, which carry the weak force. It also predicts a massless carrier of the electromagnetic force, the photon. The exact structure of the Higgs mechanism is not specified by the theory, but in any scenario, there is at least one Higgs scalar particle that survives. Other Higgs are used to give mass to the W and Z.

In 1971, Gerardus 't Hooft showed, for his PhD thesis, that as Weinberg and Salam had hoped, the Higgs mechanism did produce a theory that was renormalizable. The first experimental evidence of a neutral form of the weak interaction, called weak neutral current, was reported in 1973 from a neutrino scattering experiment. W and Z bosons were directly observed in proton-antiproton collisions in 1983. Collisions between protons are, in fact, primarily collisions between quarks. An example of W production is

$$\bar{u}d \rightarrow W^- \rightarrow e\bar{\nu},$$

where an anti-up quark and a down quark fuse to form a W which decays as before. The

Z is produced in the process

$$q\bar{q} \rightarrow Z \rightarrow e\bar{e},$$

where a quark and an antiquark of the same type fuse to form a Z which decays to an electron and a positron. The positron is almost always denoted by e^+ rather than by $\bar{e}$. Subsequently in this paper, we use the notation $Z \rightarrow ee$ in which it is implicit that ee represents an electron-positron pair.

The fourth force is the strong force. With the discovery that the nucleus of an atom is densely packed with positively charged protons, it was immediately recognized that a strong nuclear binding force was required to overcome the electromagnetic repulsive force of the positively charged protons. The discovery of the quark structure of nuclear particles led to the understanding that the strong force was a force between quarks. In quantum electrodynamics, QED, the quality which a particle has that allows it to feel the electromagnetic force is called charge and may be plus or minus. The quality which quarks have that allows them to feel the strong force is called color (and is not related whatsoever to visible color). The theory which describes the strong interaction was developed in the early 1970's and is called quantum chromodynamics, QCD, by analogy with QED. QCD is based on the symmetry group $SU(3)$ and is an unbroken symmetry as opposed to the broken symmetry of $SU(2) \times U(1)$. The carriers of the strong force are a family of eight massless gauge bosons called gluons.

The standard model is completed with a few more elementary particles. The muon was first discovered in cosmic rays and was eventually recognized as a heavy sibling of the electron. The electron and muon are classified as leptons. A third member of this group,

the tau lepton, was discovered in 1975. Each lepton has an associated neutrino, so there are three distinct neutrinos [3].

Three quarks were known at the time the quark model was postulated: up, down, and strange. It was the $SU(3)$ symmetry of the hadrons, bound states of these quarks, that originally disclosed the existence of quarks. Subsequently, the charm quark was discovered in 1974, the bottom quark in 1977, and the top quark in February 1995 [4].

The elementary particles may be arranged in three generations, see Table 1.1. The term "standard model" was first used by Abraham Pais in 1975 to describe $SU(2) \times U(1)$ theory at a time when just the first two generations of particles were known. $SU(2) \times U(1)$ accommodated the third generation without difficulty. The term "standard model" has come to include QCD as well and is sometimes referred to as $SU(3) \times SU(2) \times U(1)$. The standard model includes 12 elementary particles: 6 quarks and 6 leptons, and 12 gauge bosons: the photon which carries the electromagnetic force, the W^+, W^-, and the Z which carry the weak force, and 8 gluons which carry the strong force [3].

Gravity is not part of the standard model and is not at present successfully included in extensions to the standard model. This is for two reasons. First, the effect of gravity is inconsequential in single particle interactions since it is so much weaker than the other three forces. Second, the theories describing the other forces are written in a mathematical form called quantum field theory. One of the successes of the standard model was the unification of the electromagnetic and the weak force, called electroweak theory. Thus it has become a goal of theory beyond the standard model to unify the strong force and gravitation with the electroweak force. This unification of the forces would represent the universe as it was an instant after the Big Bang. The forces we observe in the universe today derive from the

Particle	Symbol	Charge	Mass (GeV)
Fermions			
Generation I:			
Electron neutrino	ν_e	0	$< 5.1 \times 10^{-9}$
Electron	e	-1	0.511×10^{-3}
Down quark	d	$-\frac{1}{3}$	$5 - 15 \times 10^{-3}$
Up quark	u	$\frac{2}{3}$	$2 - 8 \times 10^{-3}$
Generation II:			
Muon neutrino	ν_μ	0	$< 0.27 \times 10^{-3}$
Muon	μ	-1	0.106
Strange quark	s	$-\frac{1}{3}$	$0.100 - 0.300$
Charm quark	c	$\frac{2}{3}$	$1.0 - 1.6$
Generation III:			
Tau neutrino	ν_τ	0	< 0.031
Tau	τ	-1	1.78
Bottom quark	b	$-\frac{1}{3}$	$4.1 - 4.5$
Top quark	t	$\frac{2}{3}$	$175 - 200$
Gauge Bosons			
Photon	γ	0	0
W boson	$W^{\pm}$	± 1	80.2
Z boson	Z	0	91.2
Gluon	g	0	0

TABLE 1.1: The elementary particles

original unified force through a process called spontaneous symmetry breaking. Gravity is not as yet included in these unified theories since no one has successfully found a quantum field theory for gravity.

The predictions of the standard model have been verified by virtually all known experimental results. Yet, the standard model is generally not considered to be the most fundamental or the ultimate theory. There are, for example, at least 18 parameters that are put into the standard model by hand. This may be contrasted with general relativity that has but a single parameter. The successful unification of the electromagnetic and weak force leads to the belief that further unification may be achieved. The fact that the weak force couples only to left-handed particles is an experimental result that is put into the theory but is unexplained. It is thought by some on aesthetic grounds that physical laws must respect left-right or mirror symmetry, at least at some higher level. That is part of the motivation for the subject of this thesis, a search for new gauge bosons, W', Z', which, if they exist, could be right-handed partners of the existing W and Z.

1.3 Models for additional W, Z.

Additional heavy neutral gauge bosons, generically called Z', and heavy charged gauge bosons, W', are predicted by numerous extensions to the standard model. One of the earliest of these extensions was the addition of a right-handed gauge group to the electroweak sector giving $SU(2)_R \times SU(2)_L \times U(1)_{B-L}$. This is referred to as the left-right symmetric model and, in effect, it restores parity or mirror symmetry at higher energy. For example, the force carried by W_R, the W' of this model, would be felt by right-handed leptons or left-handed antileptons. One of the attactive features of this model is that once that right-handed

neutrinos are stipulated in $SU(2)_R$, the generator of $U(1)$ becomes $B - L$, baryon minus lepton number, which is a physical observable. In $SU(2)_L \times U(1)_Y$, the current standard model, the $U(1)$ generator is weak hypercharge, Y, which is not an independently observable physical characteristic. A second attractive feature of the left-right model is that the theory would naturally accommodate a small mass for left-handed neutrinos [5]. The mass of the W' and Z' in this model are related such that

$$\frac{m_{W'}}{m_{Z'}} = 0.5 \text{ to } 0.8$$

depending on the relative strengths of the coupling constants for $SU(2)_R$ and $SU(2)_L$ and on the structure of the Higgs sector [6].

The left-right model can also be imbedded in $SO(10)$, a higher symmetry used in a number of grand unification theories. In most $SO(10)$ theories, the symmetry-breaking scale of $SU(2)_R$ is at such a high energy that the associated W' and Z' would be beyond the reach of present or planned colliders [7]. There are, however, some $SO(10)$ models with a symmetry-breaking pattern that could make the W' and Z' accessible. A left-right model imbedded in a supersymmetric $SO(10)$ group could produce W' and Z' detectable at present or future colliders [6].

Supersymmetry is a theory which proposes a higher symmetry between bosons and fermions allowing the transformation of one into the other. One reason it is attractive is that it removes some intractable divergences (infinities) associated with the Higgs mechanism. String theory postulates that at extremely small distances, the Planck scale, fundamental particles are represented mathematically as one-dimensional strings rather than zero-dimensional points. Strings can generate the types of fundamental particles found in

nature including gravitons, the carrier of the gravitational force, thus string theory became a natural framework for a unified theory. The supersymmetric version of string theory, superstring theory, leads to the gauge groups of existing unified theories and determines the number of space-time dimensions as well [5]. It has generated an enormous amount of theoretical interest but progress has been slow.

E_6 is the next natural symmetry group for a unified theory beyond $SO(10)$. It has generated a lot of theoretical interest because it is the simplest unifying group compatible with superstring theory [8]. In one version, E_6 decomposes into a form of $SU(2)_R \times SU(2)_L \times U(1)$ called the alternative left-right symmetric model [9]. This model also predicts a W' and Z' that could be detected at present or future colliders.

There are many other decompositions of E_6 that lead to additional $U(1)$ symmetry groups. These theories do not predict additional charged bosons but may include one or more additional neutral bosons, Z' [6].

There are a number of other models that predict additional gauge bosons, but most theoretical interest and hence most phenomenological studies relate to the models or variations of the models discussed above. To summarize, most unified theories predict Z' and some include W' as well. In a number of these theories, the Z' and W' could be detectable at present or planned colliders.

1.4 This study

In this thesis, we will report the results of a direct search for W' and Z', We will specifically look for the decay products of W' and Z' formed in $p\bar{p}$, proton-antiproton, collisions. In the absence of evidence for these processes, we will set limits on the production

cross section for W' and Z'. We also set a lower bound on the mass of a W' and a Z'. To set such a limit, it is necessary to choose a particular model. We choose reference models that are traditionally used for this purpose. For the W', we take the coupling strength and the CKM mixing matrix to be the same as in the standard model and further assume no $W - W'$ mixing. For example, if W' is W_R, we assume exactly the same couplings as in the standard model except left-handed fermions are replaced by right-handed ones. This type of W_R is compatible with theory but most of these restrictions are not set by theory so the mass limit for many types of W_R could be significantly lower [10].

For the Z' reference, we also choose the same couplings to quarks and leptons as the standard model Z. There is no theoretical model for a Z' of this type but it is a traditional and useful reference [7]. All specific Z' models are expected to have smaller cross sections than this model so mass limits for specific Z' can be substantially less [11]. Mass limits in this paper will refer to reference model W' and Z'. For both the reference model W' and Z', we assume that decay to W and Z is suppressed.

A number of indirect searches for W' have been carried out in the past. Muon decay has been carefully studied looking for deviations from V-A behavior as an indication of W', valid when $m_\nu < m_\mu$ [12]. Constraints on additional W bosons are also obtained from the mass difference between K_S and K_L, Δm_K [13]. $B_d - \bar{B}_d$ mixing also limits extra charged gauge bosons [14]. The semileptonic branching ratio $b \to X l \nu$ may be used to set a limit if $m_\nu > m_b$ [15]. The above results may be combined to exclude W' lighter than 1.3 TeV. However, if right-handed CKM matrix is allowed to take on other reasonable values, a limit of $M_{W'} > 300$ GeV can be consistent with these experimental results, still assuming equal coupling strengths for $SU(2)_R$ and $SU(2)_L$ [10]. Cosmological nucleosynthesis studies have

established a limit $m_{W'} > O(1\ \text{TeV})$ if $m_\nu < 1$ MeV [16]. Analysis from the supernova 1987A, valid for a neutrino lighter than 10 MeV, excludes $m_{W'}$ less than 16 TeV [17]. One analysis, however, combines several different experimental results and indicates a W' with a mass ≈ 230 GeV, given a small mixing angle [18]. Previous direct searches in $p\bar{p}$ collisions have set the limit $m_{W'} > 652$ GeV [19].

Indirect limits on Z' coming from weak neutral current experiments, precision measurement at the Z pole, and the W mass measurement may be combined to exclude a reference model Z' with mass less than 750 GeV. The same data would exclude a Z' from an E_6 model with a mass less than 180 GeV [7]. Previous direct searches in $p\bar{p}$ collisions have set a limit, $m_{Z'} > 505$ GeV [20].

In this paper, we report a direct search with the DØ detector for a heavy ($m_{W'} > m_W$) charged gauge boson decaying through the channels $W' \to e\nu$ and $W' \to \tau\nu \to e\nu\nu\bar{\nu}$. Limits are set on the cross section times branching ratio, σB, for $W' \to e\nu$ assuming that the neutrino from W' decay is stable and has a mass significantly less than the W' mass. The branching ratios $W' \to e\nu$ and $W' \to \tau\nu$ were taken to be equal.

Most charged gauge bosons decaying leptonically ($W(W') \to l\nu$) may be identified from the projection of the event onto the plane perpendicular to the beam direction (transverse plane). Candidate events are selected by demanding a lepton with large transverse energy, E_T, in an event with large missing transverse energy, $\not{E}_T$, carried away by the undetected neutrino. In the present study only $W(W')$ decay channels which include an electron in the final state are considered. Transverse mass is defined as the mass of the electron-neutrino system taking into account only the vector components in the transverse plane. In general, the method of search is to look in the transverse mass spectrum for the line shape of a W'

superimposed on that expected from the standard model W boson. The analysis presented here is based on data collected during the Fermilab Tevatron $p\bar{p}$ collider run from August 1992 to May 1993, run 1a, with an integrated luminosity of 13.5 pb^{-1} at $\sqrt{s} = 1.8$ TeV.

We also report a search for Z' in the decay channel, $Z' \rightarrow ee$. We will set a limit on σB for $Z' \rightarrow ee$. The invariant mass of the ee pair is reconstructed from the 4-momenta of the two electrons. The method of search is similar to that of the W'. We look in the invariant mass spectrum for the Breit-Wigner peak of a Z' superimposed on the invariant mass spectrum expected in the standard model arising from Z and Drell-Yan production. The data is from the same collider run, run 1a. For this analysis, the integrated luminosity is 14.5 pb^{-1}.

Chapter 2

Experimental apparatus

2.1 The Tevatron

The Tevatron, the world's highest energy particle collider, is located at Fermi National Accelerator Laboratory, Fermilab, about 40 miles west of Chicago. Counter-rotating bunches of protons and antiprotons are each accelerated to 900 GeV to produce $p\bar{p}$, proton-antiproton, collisions with a center of mass energy $\sqrt{s} = 1.8$ TeV. The first $p\bar{p}$ collisions in the Tevatron occurred in 1985. The bunches are contained in a highly evacuated non-magnetic oval stainless steel pipe about 3 inches wide by 2 inches high. The pipe forms a circle 1000 meters in radius, or about 4 miles in circumference. It is located in a tunnel several meters underground. The beam pipe is surrounded for substantially its entire length by 774 bending dipole magnets and 216 focusing quadrupole magnets. The magnets are niobium-titanium alloy, superconducting at 4.6 K. They are maintained at this temperature by being emersed in liquid helium. The magnets maintain a field strength of 4 Tesla in the beam pipe.

There are six almost evenly spaced bunches of protons and six bunches of antiprotons in the beam pipe when the Tevatron is in colliding mode. For an instantaneous luminosity of 10^{31} cm^{-2}s^{-1}, there are approximately 18×10^{10} protons per bunch and 6×10^{10} antiprotons per bunch. Since protons and antiprotons have opposite charge, it is possible to maintain the orbits of the p and $\bar{p}$ bunches moving in opposite directions in the same beam pipe with the same magnetic field. Special quadrupole magnets at either side of the interaction area focus the beams into a luminous region narrowing the beam width to a diameter of

0.1 mm. Collisions occur where the focused p and $\bar{p}$ beams intersect. The particle detector is designed to have this interaction point at its center, that is in so far as possible to be symmetric with respect to this point. In actuality, the interaction region is spread out over a large distance longitudinally in the beam direction. This is due to the fact that p and $\bar{p}$ bunches are spread out. Proton-antiproton collisions had a distribution of ± 27 cm in run 1a. The center of the distribution was also offset 8 cm from the center of the detector due to an alignment error in the focusing magnets.

A proton and antiproton bunch intersect within the detector every 3.5×10^{-6} seconds. The inelastic cross section for $p\bar{p} \rightarrow X$ is ≈ 60 mb. The number of expected $p\bar{p}$ collisions per crossing, $\bar{n}$, is given by $\bar{n} = \sigma L T$ where σ is the cross section, L the instantaneous luminosity, and T the time between bunch crossings. For $L = 10^{31}$, $\bar{n} = 2$. For run 1a, L ranged from 1×10^{30} to 8×10^{30}, so $\bar{n}$ ranged from 0.2 to 1.6. The distribution of events per crossing is given by the Poisson probability distribution. In typical operation during run 1a, a $p\bar{p}$ collision would be expected in about one half of the bunch crossings.

Protons, which begin life at Fermilab as a bottle of hydrogen, go through four sequential accelerators before reaching the Tevatron, see Fig. 2.1. In the first stage, H^- ions are extracted from a cathode and accelerated through an electrostatic potential to 750 KeV. In the remaining stages and in the Tevatron, acceleration is accomplished by radio frequency fields. The second stage is a linear accelerator, linac, in which the H^- ions are accelerated to 400 MeV through a series of radio frequency acceleration gaps.

The 400 MeV H^- ions next enter the Booster. The Booster is a circular synchrotron, 75 meters in radius. The H^- ions are stripped of their electrons by a carbon foil becoming free protons as they enter the Booster. The proton bunches are accelerated to 8 GeV and

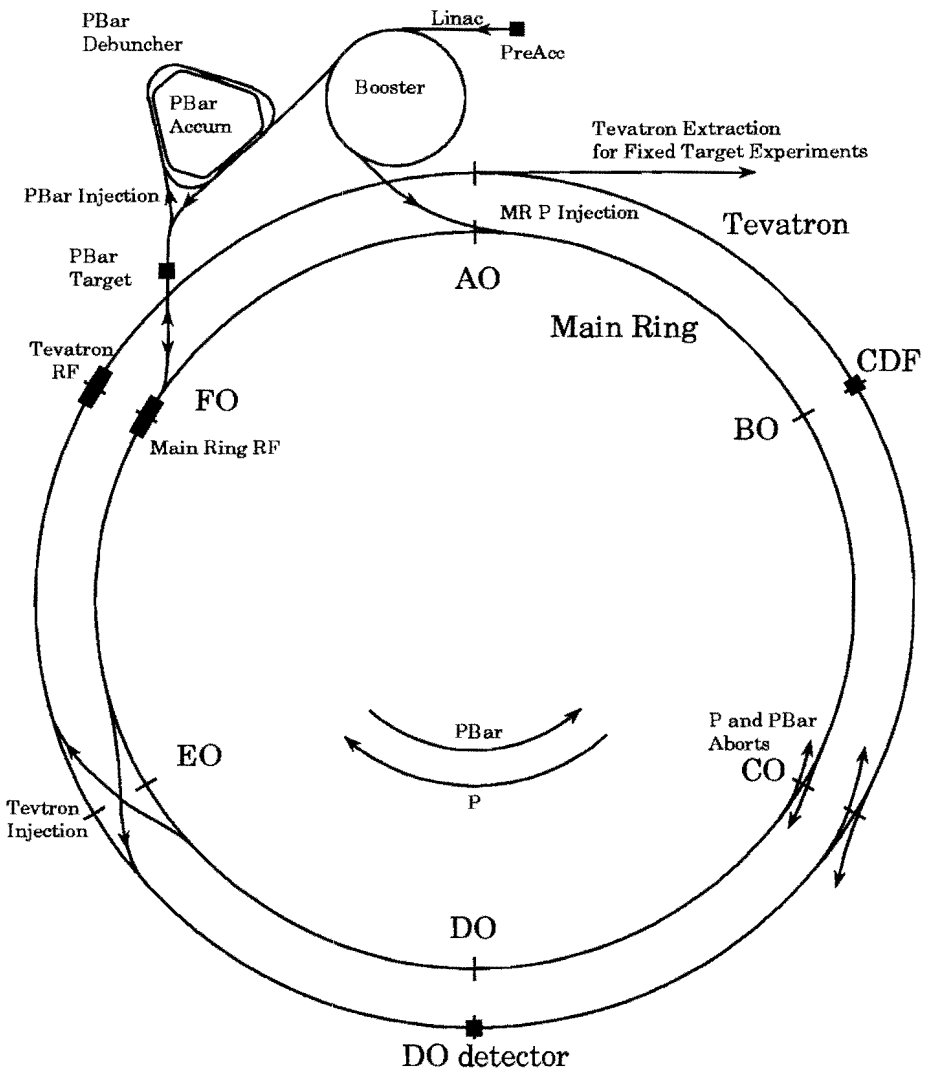

FIG. 2.1: A schematic drawing of the Fermilab collider, not to exact scale. In particular, the Tevatron and the Main Ring both have a radius of 1,000 meters.

injected into the Main Ring.

The Main Ring has the same radius as the Tevatron (1000 meters) and is located in the same tunnel directly above it. The Main Ring was the first accelerator built at Fermilab and employes non-superconducting magnets. It is capable of accelerating protons to 400 GeV for fixed target operation. The fixed target experimental program is conducted separately and does not overlap collider operations. The Main Ring serves two functions when Fermilab is operating as a collider. The first function of the Main Ring is to act as an injector for the Tevatron. The 8 GeV protons received from the Booster are coalesced into a single bunch, accelerated to 150 GeV, and injected into the Tevatron. The process is repeated until all six proton bunches are in the Tevatron. The process is then repeated using 8 GeV antiprotons which are extracted from the antiproton accumulator. Once the Tevatron contains six proton and six antiproton bunches at 150 GeV, the Tevatron accelerates the bunches to 900 GeV. The p and $\bar{p}$ bunches are sometimes referred to collectively as the beam.

Once the beam is at 900 GeV, it is squeezed and scraped. Then $p\bar{p}$ collisions and data taking begin. The entire procedure up to this point is called a shot setup and typically takes about one hour. Once the shot setup is complete, the initial p and $\bar{p}$ bunches cannot be replenished and the instantaneous luminosity gradually decreases. The period of time after shop setup in which $p\bar{p}$ collisions occur is called a store. A typical store lasts approximately 18 hours.

During a store, the Main Ring perform its second function which is to generate antiprotons. Protons are produced as before and 8 GeV protons are transferred from the Booster to the Main Ring. They are accelerated to 120 GeV and directed into a nickel target. The

120 GeV beam energy is selected to maximize the production of 8 GeV antiprotons. The collision debris is collimated by a lithium magnetic lens. The collision debris including antiprotons is directed into the debuncher by being passed through a dipole magnetic field which selects 8 GeV negatively charged particles. Particles other than antiprotons eventually decay. One bunch of $\approx 10^{12}$ protons collides with the nickel target every 2.4 seconds producing $\approx 10^{7}$ antiprotons. The debuncher uses the 2.4 seconds until the next batch of antiprotons arrives to reduce the momentum spread and to reduce the lateral oscillations through a process known as stochastic cooling. The antiprotons are then transferred to the antiproton accumulator to await the next shot setup.

The process of creating antiprotons is called stacking. The stack rate is $\approx 5 \times 10^{10}$ antiprotons per hour. Since the efficiency of transferring antiprotons from the antiproton accumulator through the Main Ring into the Tevatron is about 50%, it takes most of the store duration to accumulate enough antiprotons for the next store.

There are two places on the Tevatron ring at which the beam is tightly focused to allow $p\bar{p}$ collisions, B0 and D0. The CDF, Collider Detector at Fermilab, experiment is located at B0. The DØ experiment takes its name from its Tevatron "street address", D zero [21].

2.2 The DØ detector

The DØ collaboration, a collaboration of more than 400 physicists from 40 universities and research institutions in nine countries, designed, built, and operates the DØ detector. The DØ detector is a 4π detector, that is, it completely surrounds the interaction spot symmetrically in so far as possible. The symmetry is of necessity cylindrical since the beam passes through the detector. The detector is described in cylindrical coordinates –

r, ϕ, and z – with the z axis coincident with the beam. The $\bar{p}$ beam comes from the $+z$ direction and $z = 0$ is at the nominal center of the interaction area. The ray $\phi = 0$ is in the horizontal plane and directed toward the center of the ring. Pseudorapidity, η, is defined $\eta \equiv \tanh^{-1}(\cos\theta)$ where θ is the polar angle, see Fig. 2.2. Locations in the calorimeter are commonly specified in $\eta - \phi$ space, $-\infty < \eta < \infty$, $0 < \phi < 2\pi$. As used in this paper, η refers to detector η calculated from $z = 0$. The physics η of a particle is calculated from the location of the interaction along the z axis which is in general not at $z = 0$.

The detector consists of three main subsystems: a central detector, a calorimeter, and a muon detection system, see Fig. 2.3.

2.2.1 The central detector

The central detector occupies the innermost cylindrical volume of the detector, $r = 78$ cm, $z = \pm 135$ cm. The primary purpose of the central detector is to locate tracks from charged particles. Tracks are identified within $|\eta| < 3.1$. The calorimeter, which surrounds the central detector, makes accurate measurement of the energy and position of particles. The position coordinates are detector η and ϕ. To translate this information into a physics event, it is necessary to find the z coordinate of the primary event vertex. It is sufficient to assume $r = 0$ for the event vertex. Given the z vertex, detector η may be translated to physics η. Then energy clusters in the calorimeter may be expressed as 4-vectors, assuming that all particles are relativistic, hence massless, using:

$$E_z = \frac{E}{\tanh\eta}, \; E_T = \frac{E}{\cosh\eta}, \; E_x = E_T\cos\phi, \; E_y = E_T\sin\phi.$$

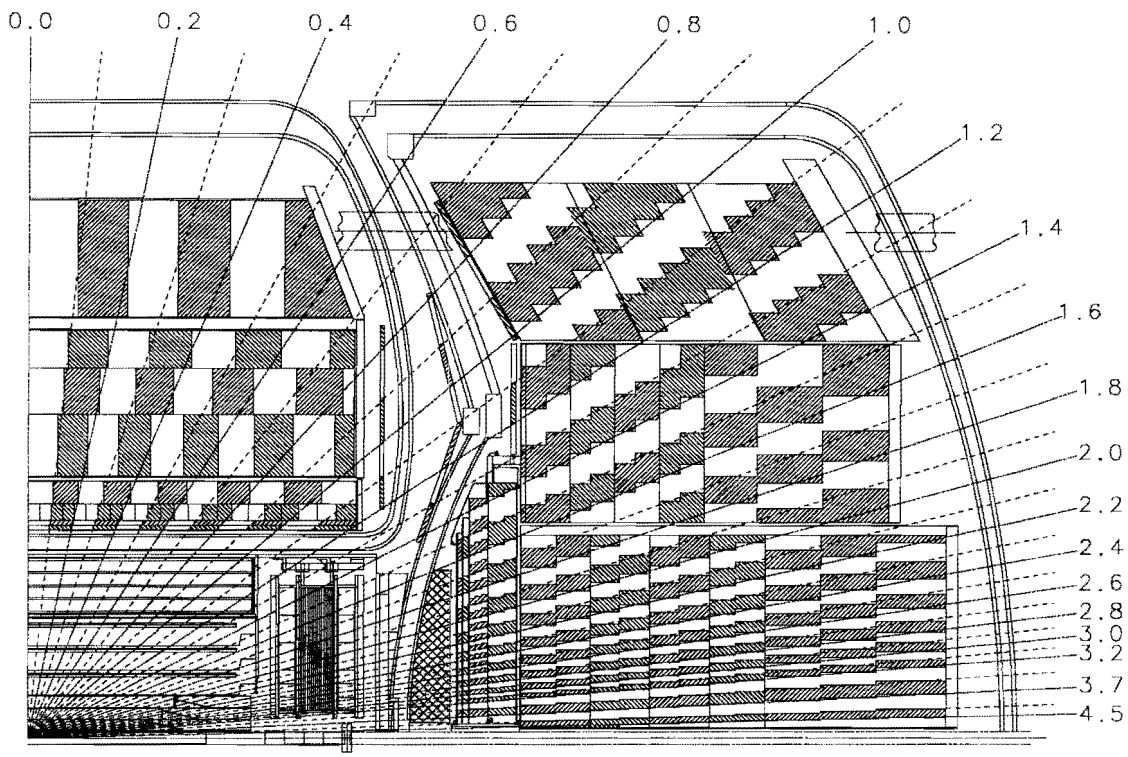

FIG. 2.2: A one quarter section schematic of the central tracking system and the calorimeter. The center of the detector is the lower left corner. The angular units are pseudorapidity, η.

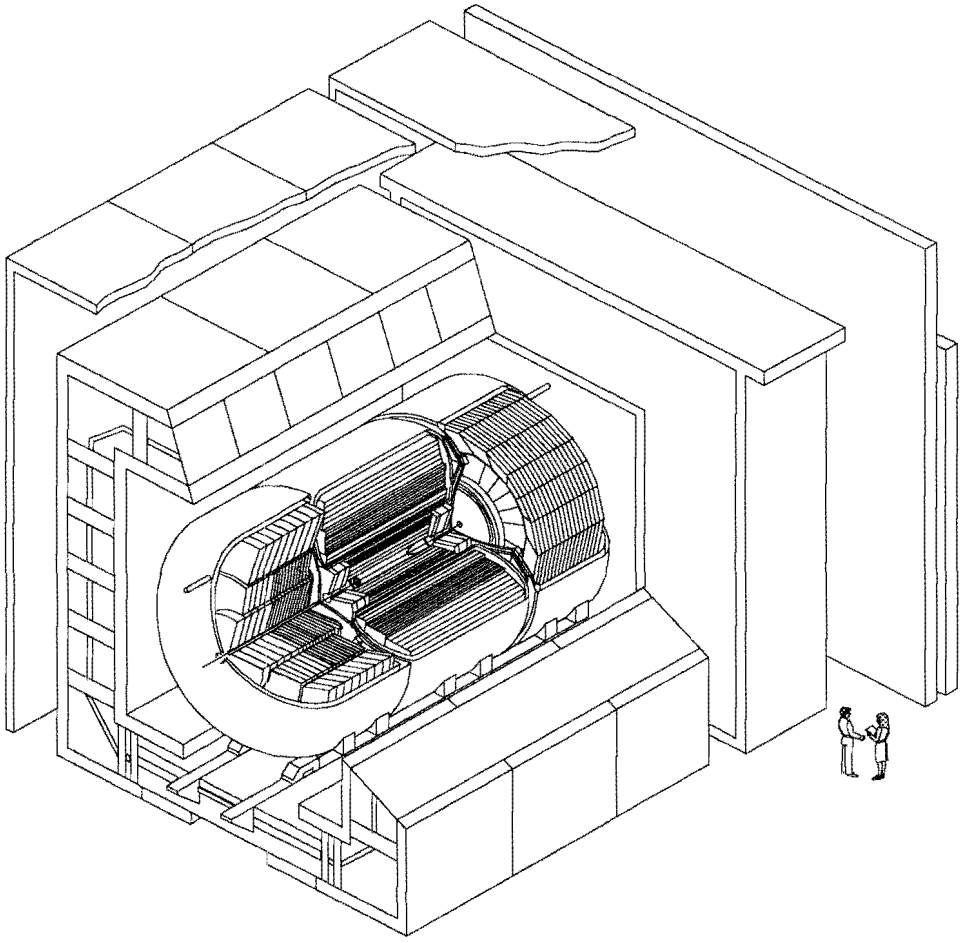

FIG. 2.3: A cut away view of the DØ detector. The external rectilinear structure is the toroidal magnets and drift tubes of the muon detection system. The large cylindrical structure is the calorimeter. The innermost cylinder is the central tracking system.

Therefore, the primary benefit of track finding is to locate the z vertex. The second purpose is to associate tracks with energy recorded in the calorimeter. For example, given a highly electromagnetic energy cluster in the calorimeter, the absence of a track would indicate that the track came from a photon while the presence of a track would indicate it came from an electron.

The central detector consists of four subsystems: the vertex chamber, VTX, the central drift chamber, CDC, the forward drift chambers, FDC, and the transition radiation detector, TRD, see Fig. 2.4. The VTX, CDC, and FDC are wire drift chambers. A charged particle traversing the chamber will ionize the gas in the chamber. An electrostatic field causes the liberated electrons to drift to sense wires. The resulting currents are read out through preamplifiers, shaped, and then digitized. This comprises the first stage of the data acquisition system. The VTX has a resolution in the ϕ direction of 0.06 mm. The z resolution provided by charge division from the sense wires is 15 mm. In the CDC, the position resolution in ϕ is 0.18 mm. The z resolution provided by delay lines is 2.9 mm. The FDC provides resolution in ϕ of 0.2 mm and in θ of 0.3 mm.

The TRD operates on the principle that an ultrarelativistic particle will radiate photons, x-rays, when crossing the boundary between materials with different dielectric constants. Since the intensity of the radiation is proportional to the Lorentz boost γ, one can discriminate between electrons and pions since the pion is 270 times heavier than the electron. A similar discrimination can be achieved using energy loss information from the tracking chambers. Both of these techniques reduce the background from fake electrons at some loss in efficiency. Neither technique was needed in this analysis.

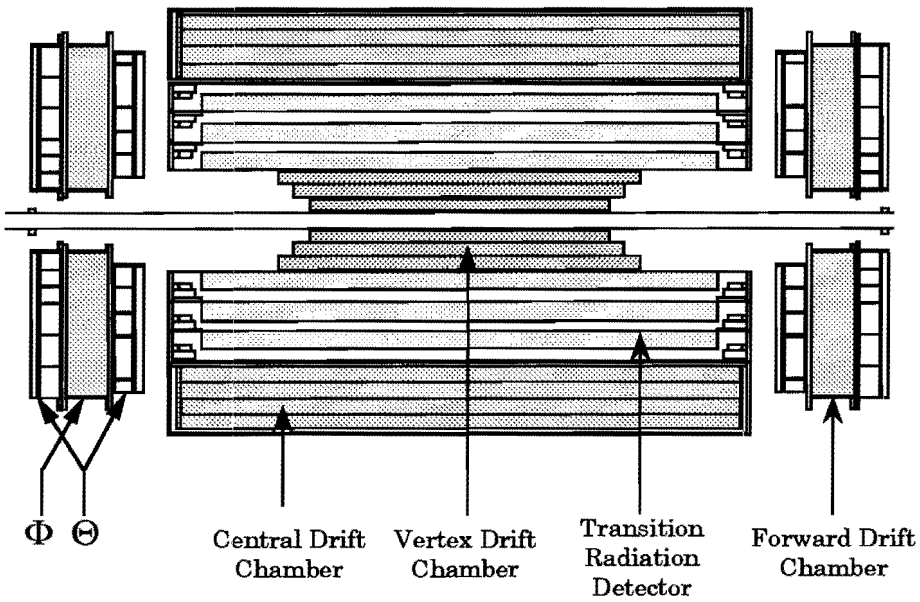

FIG. 2.4: The central tracking system.

2.2.2 The calorimeter

In many colliding detector designs, there is a central, uniform magnetic field generated in most cases by a solenoidal magnet located just outside the tracking volume. The tracks from charged particles are curved in such a field and a momentum measurement can be made from the curvature. A solenoidal magnet as well as a complete new tracking system is planned for the upgraded DØ detector in 1998. For run 1a and the current run, 1b, the only measurement of energy comes from the calorimeter. All decay products are measured by the calorimeter except for muons and neutrinos. Muons are detected by the muon system located outside the calorimeter but leave a dE/dx trace in the calorimeter which aids in their identification. The presence of neutrinos is inferred from missing transverse energy in the calorimeter.

The calorimeter consists of sheets of absorber with intervening ionizing material. Showers containing charged particles originate in the absorber. The passage of charged particles through ionizing material generates free electrons which drift through an electrostatic field to sense pads. The detection of the current from the sense pads is conceptually similar to the detection of the signal from the drift chambers. Electromagnetic particles, electrons and photons, interact with the absorber through the electromagnetic force and shower readily through the processes $e \rightarrow \gamma e$ and $\gamma \rightarrow ee$. Hadrons interact with the absorber by interacting with the nucleus via the strong force. A greater thickness of absorber is required to induce hadron showers. Incident hadrons, predominantly charged pions, produce more pions on interacting with the absorber. A substantial fraction of these pions are neutral pions which immediately decay to two photons producing electromagnetic showers within

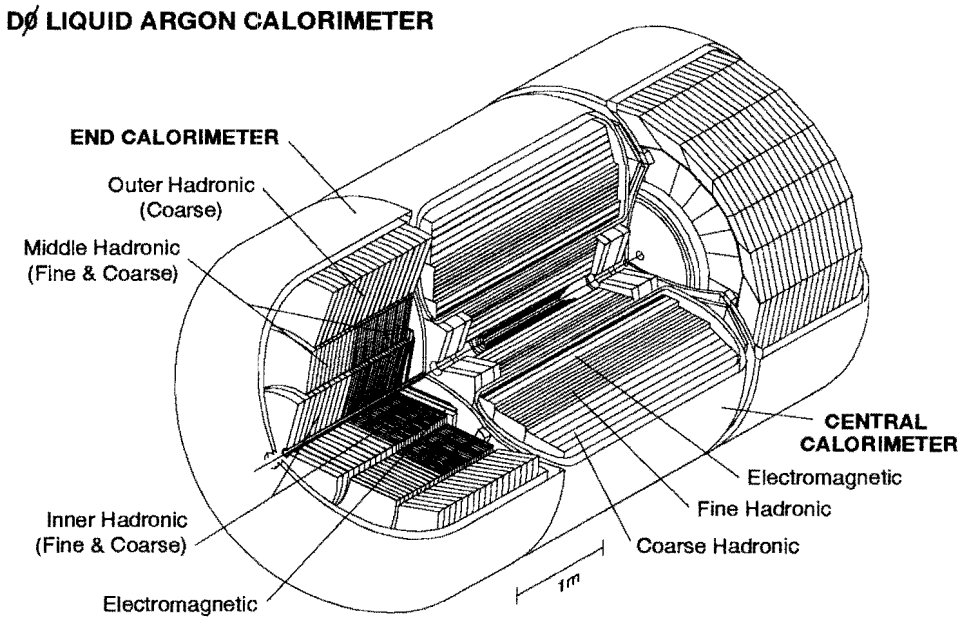

FIG. 2.5: A cut away view of the liquid argon calorimeter.

the hadron shower. The shower profile of hadronic showers is more spread out in the lateral direction and in depth than that of electromagnetic showers.

The calorimeter works on the principle that the strength of the current read out is proportional to the incident energy of the particles. By choosing the appropriate thickness of the absorbing material, the DØ calorimeter is designed so that about 95% of the electromagnetic energy is contained in the first four layers. This is called the EM section and very little hadronic energy is deposited here. The next three layers constitute the fine hadronic section, FH, and the final layer is the coarse hadronic section, CH, see Fig. 2.5. The DØ calorimeter uses uranium for absorber in the EM and FH sections and stainless steel or copper in the CH. Liquid argon is used as the ionizing medium. This requires cryostats to maintain the calorimeter at 78K. In order to reduce the uncertainly in the energy measurement, it is desirable to have the electron/pion, e/π, response of 1. For the DØ calorimeter,

e/π varies from 1.11 at 10 GeV to 1.04 at 150 GeV.

The DØ calorimeter is hermetic, providing full coverage to $|\eta| < 4$, see Fig. 2.2. The calorimeter consists of three modules, a central barrel calorimeter, CC, and two end caps, EC. In the gap between the modules, spatial resolution deteriorates substantially but an intercryostat detection system prevents energy loss.

The lateral segmentation is such that the calorimeter is arranged approximately in projective towers. The lateral segmentation in all layers except EM3 is 0.1×0.1 in $\eta - \phi$ coordinates except at large $|\eta|$. In the third EM layer, EM3, in which the EM shower is at maximum intensity, the segmentation is 0.05×0.05 to give finer spatial resolution. The EM section is 20.5 radiation lengths in depth. In the CC, the depth in interaction lengths is 0.76 in the EM section, 3.23 in the FH, and 3.17 in the CH. The depth in interaction lengths is somewhat greater in the EC.

2.2.3 The muon system

The muon detection system surrounds the calorimeter. It consists of three sets of multilayer proportional drift tubes, one before and two outside a toroidal magnetic field. Coverage is provided to $|\eta| < 3.6$. The muon system is only used in this analysis to help identify cosmic ray muons which bremsstrahlung – radiate an energetic photon – and deposit electromagnetic energy in the calorimeter.

2.2.4 The trigger

The function of the triggering system is to reduce the event rate which ranged from 50k to 250k per second (Hz) during run 1a to 2 Hz by selecting interesting events. The

level 1 trigger is called a hardware trigger. It consists of a series of 32 programmable logical circuits that each test an array of up to 256 logical conditions based on information in the event. A positive decision from any of the 32 level 1 triggers causes the event to be accepted. The event rate out of level 1 is $\approx$ 200 Hz. Level 1.5, which operates on muon information, reduces that rate to $\approx$ 100 Hz. The level 2 trigger is a farm of microprocessors, each handling one event at a time. A partial event reconstruction is performed. Up to 64 level 2 triggers, sets of trigger conditions often called filters, were allowed in run 1a. Level 2 reduces the event rate to $\approx$ 2 Hz for capture on magnetic tape [22].

Chapter 3

W' search

3.1 Data sample

The event sample for the W' search is selected from the full run 1a data set. The events were processed with the event reconstruction program DØRECO versions 11.17, 11.18, and 11.19. The luminosity for this sample for the trigger used in this analysis, ELE_MAX, is 13.5 pb^{-1}. Electron energy, jet energies, and missing transverse energy, $\not\!\!E_T$, are corrected after event reconstruction. The electron energy is calibrated using the Z boson mass. The electron energy is scaled by the following factors: 1.072 CC, 1.025 EC north, and 1.012 EC south. The uncertainty in the electron energy scale is 0.5%. The jet energy scale was set by requiring energy balance in events with a normal hadronic jet and a predominantly electromagnetic jet or photon. The uncertainty in the jet energy scale is 6%. The average correction to jet energies is $\approx +23\%$. $\not\!\!E_T$ is computed using corrected electron and corrected jet energies. The corrected jets used for this purpose have a cone radius $R = 0.7$ in η, ϕ coordinates. This R is the largest cone radius available in the reconstructed events and is chosen to minimize the remaining uncorrected energy in the event. The uncertainty in $\not\!\!E_T$ is $1.08 + 0.019 \times \sum E_T$ (GeV) based on minimum bias data [23].

3.2 Event selection

The following criteria are used to select $W(W')$ candidates. The level 2 trigger ELE_MAX is required. ELE_MAX is defined as follows. In the associated level 1 trigger, events are required to have at least one electromagnetic trigger tower of size 0.2×0.2

$(\Delta\eta \times \Delta\phi)$ with E_T greater than 10 GeV. In level 2 where clusters are reconstructed, a cluster with $E_T > 20$ GeV fulfilling isolation and electromagnetic shape criteria is required. In addition, $\not{E}_T$ must be greater than 20 GeV.

The following kinematic cuts are applied after event reconstruction: electron transverse energy $E_T^e > 30$ GeV and $\not{E}_T > 30$ GeV. The values were chosen with these goals: to be safely above trigger thresholds, to reduce the QCD background (discussed in 3.4) and thereby reduce the associated large uncertainty, and to not cut too far into the Jacobian peaks of these distributions where substantial W signal is expected.

Electrons are required to be well isolated and are further identified using shower shape criteria determined from test beam and collider data. These cuts discriminate against jets with substantial electromagnetic energy. Electromagnetic energy in a jet is generally not well isolated. Isolation is defined:

$$I \equiv \frac{E_{T,R=.4} - E_{T,R=.2}^{EM}}{E_{T,R=.2}^{EM}},$$

where R is the cone radius and EM refers to the EM section of the calorimeter.

A covariance matrix of 41 parameters describing the electromagnetic shower shape as a function of position in the calorimeter is determined from simulated electron showers. The simulation is tuned to agree with test beam data. The H-matrix is the inverse of the covariance matrix. The H-matrix χ^2 is determined from the fit of the shower shape of the event to the H-matrix. A unitary transformation which diagonalizes the symmetric H-matrix is performed on the 41 parameter input vector and on the H-matrix so that the fit is made with uncorrelated variables [23].

Electromagnetic fraction is defined:

$$\text{EM fraction} \equiv \frac{E^e - E^{FH1}}{E^e + \text{additional associated hadronic energy}}.$$

E^{FH1} refers to energy in the first layer of the fine hadronic section of the calorimeter. Since only energy from the EM layers and FH1 is included in the electron clustering algorithm, the numerator above is the electron energy in the EM layers.

There must be a well defined track in the central tracking system connecting the event vertex and the electromagnetic energy cluster in the calorimeter. Track match significance is defined:

$$\text{Significance} \equiv [(\frac{\Delta z}{\delta z})^2 + (\frac{\Delta \phi}{\delta \phi})^2]^{\frac{1}{2}},$$

in the CC, where δz and $\delta \phi$ are the resolutions of those variables. In the EC, substitute θ for z.

The following requirements are applied to identify electrons. The cuts are kept loose so that the selection efficiency will be relatively high, a desirable feature for a new particle search. The cuts are loosened to the point where in the high transverse mass tail of the W, the ratio of W signal to QCD background is about 1:1.

- Isolation < 0.15.
- Electromagnetic fraction > 0.9.
- H-matrix $\chi^2 < 100$, CC (200, EC).
- Number of associated tracks > 0.
- Track matching significance (SIG)< 10.

Electrons are also required to be in the fiducial region of the calorimeter. For the CC, the requirement is $|\eta| < 1.1$. Additionally, the CC is composed of 32 ϕ modules, each covering an arc of $2\pi/32$. The distance from the shower center to the nearest module edge must be > 0.01 radians in ϕ. This reduces the CC fiducial area by $\approx 10\%$. In the EC the fiducial region is $1.5 < |\eta| < 2.5$. There are no module boundaries. It is further required that the z coordinate of the primary vertex be within 100 cm of $z = 0$.

Additional cuts are applied to reject events with mismeasured $\not\!\!E_T$ due to electronic noise or accelerator background. Events with hot cells are removed during event reconstruction. If, after hot cell removal, the energy distribution by calorimeter layer within a jet is extreme, then the jet is considered to be due to noise and the $\not\!\!E_T$ in the event is suspect. For this analysis, jets are defined with a cone $R = 0.5$ to be compatible with other electroweak analysis. For each jet in the event with $E_T > 20$ GeV, the fractional energy in the EM section must be greater than 5% and the fraction in the coarse hadronic CH section less than 40%, otherwise the event is rejected. To reject spurious electron signals, the number of calorimeter cells included in the electron cluster must be greater than 20.

3.3 Selection efficiency

3.3.1 Kinematic and geometric acceptance

The PYTHIA event generator version 5.7 [24] is used throughout this analysis to generate W and W' ($m_{W'} > m_W$) events. The MRS D$-'$ [25] parton distribution functions (pdf's) are used. They were found to agree well with experimental results [26]. The MRS D0$'$ and CTEQ 2M [27] pdf sets are used as required to estimate the uncertainty in that

choice. The kinematic and geometric acceptance is 33.9 ± 0.7% for $W \to e\nu$ and 0.7 ± 0.02% for $W \to \tau\nu \to e\nu\nu\bar{\nu}$. (For a W' with $m_{W'} = 600$ GeV, the kinematic and geometric acceptance is 72.6 ± 1.6% for $W' \to e\nu$ and 14.0 ± 0.4% for $W' \to \tau\nu \to e\nu\nu\bar{\nu}$.) The kinematic and geometric acceptance by calorimeter unit is:

- $W \to e\nu$
  - CC: 0.234 ± 0.005
  - EC: 0.106 ± 0.003
- $W \to \tau\nu \to e\nu\nu\bar{\nu}$
  - CC: 0.0045 ± 0.0002
  - EC: 0.0020 ± 0.0002.

The error arises primarily from pdf uncertainty. Subsequent efficiencies are determined within the kinematic and geometric acceptance, unless noted.

3.3.2 Trigger efficiency

The trigger efficiency has been previously calculated for ELE_HIGH for electron $E_T >$ 25 GeV [28]. It is assumed that there is no statistically significant improvement when the E_T threshold is moved to 30 GeV. Since the W trigger, ELE_MAX, is a subset of ELE_HIGH, we may calculate the marginal efficiency for ELE_MAX and multiply by the efficiency for ELE_HIGH to get the total efficiency. The trigger ELE_HIGH only requires electron quality whereas ELE_MAX also requires $\not\!\!E_T$. The $\not\!\!E_T$ requirement is assumed to be uncorrelated. ELE_HIGH had two definitions during run 1a and only runs where the

electron selection criteria are the same for ELE_HIGH and ELE_MAX are used for this calculation. The efficiency for ELE_MAX given ELE_HIGH may be determined by looking at the W sample since all events that pass ELE_HIGH and meet W selection criteria are included. The efficiencies are:

- ELE_HIGH
  - CC: 0.988 ± 0.008
  - EC: 0.990 ± 0.010
- ELE_MAX given ELE_HIGH
  - CC: 0.994 ± 0.001
  - EC: 0.988 ± 0.003
- ELE_MAX (combined)
  - CC: 0.982 ± 0.008
  - EC: 0.978 ± 0.011.

The trigger ELE_MAX or the equivalent is required in subsequent efficiencies.

3.3.3 Event reconstruction efficiency

The contribution of E_T^e and $\not{E}_T$ resolution effects on reconstruction efficiency is modeled by Monte Carlo. The generated events are passed through a detector simulator which uses parameterized DØ calorimeter energy resolution. A fast Monte Carlo [29] was implemented to simulate the segmentation of the DØ calorimeters. The code places final state particles into the corresponding electromagnetic or hadronic calorimeter cells. The energy deposited

	Constant α (%)	**Sampling** β ($\%\sqrt{\text{GeV}}$)	**Noise** δ (GeV)	**Angular Resolution (radians)**
Electromagnetic				Theta
CC	1.0	13.0	0.4	0.055
EC	0.3	16.0	0.4	0.024
Hadronic				Phi
CC	4.0	40.0	0.0	0.008
EC	4.0	40.0	0.0	0.026
ICD	4.0	120.0	0.0	

TABLE 3.1: Parameters used in the fast Monte Carlo for calorimeter energy resolution and the angular resolution for electrons.

in each of these cells is smeared according to the resolution in CC, EC, and IC (inter-cryostat) regions with the following formula:

$$\frac{\sigma_E}{E} = \alpha \oplus \frac{\beta}{\sqrt{E_s(\text{GeV})}} \oplus \frac{\delta}{E(\text{GeV})}$$

where E_s is $E_T(E)$ for CC(EC/IC) [30,22]. The hadronic and IC resolutions were partially tuned to match the data. The electron position is smeared by the angular resolution. The parameters α, β, δ, as well as the angular resolution for electrons are given in Table 3.1 for the different calorimeters.

The program also introduces hadron energy degradation. This means that the actual hadronic energy entering a given tower is scaled down to simulate the energy measured experimentally. A scale factor equal to 0.83 was used in this analysis. The interaction vertex position is shifted to $z = -8.5$ cm and smeared with $\sigma_z = 26.8$ cm to match the experimental conditions.

In the fast Monte Carlo, jets are reconstructed with a simple algorithm based on the

routine LUCELL used in the PYTHIA package. Electrons are defined as in the data but using only EM fraction and isolation. H-matrix χ^2 is not used since shower profiles are not simulated.

The reconstruction efficiency due to energy resolution effects is:

- CC: 0.976 ± 0.010
- EC: 0.920 ± 0.011.

The error is principally the systematic error on $\not\!\!E_T$ resolution.

The electron identification efficiency is taken from the Z sample which has a selection cut on isolation, $I < 0.15$. The efficiency of this cut is taken from Ref. [31]. That study uses the same trigger but uses $E_T^e > 25$ GeV and DØRECO, version 10.12. The effect of this difference is assumed to be small. The efficiency for $I < 0.15$ is:

- CC: 0.985 ± 0.005
- EC: 1.00 ± 0.008.

The efficiency for selecting events with $\chi^2 < 100$ CC (200 EC) and track match significance, SIG, < 10 is determined by looking at Z candidates. The invariant mass m_{ee} is required to be in $m_Z \pm 10$ GeV. One electron at a time is fixed and required to pass very tight cuts: $\chi^2 < 100$, $I < 0.1$, and $SIG < 5$. The cut on the other electron is varied and the effect observed. The QCD background in the sample is estimated using dijet events in the same manner as for the Z sample. The effect of subtracting the background is to increase the measured efficiency by 0.003, CC, and 0.004, EC. The efficiency given $I < 0.15$ for the cut $\chi^2 < 100$ CC (200 EC) and $SIG < 10$ is:

- CC: 0.907 ± 0.011

- EC: 0.873 ± 0.022.

The track finding efficiency is determined from the Z sample requiring m_{ee} in $m_Z \pm 10$ GeV and $I < 0.15$. The QCD background is determined from dijets and subtracted. In the following, ee indicates that both electrons have a matching track and γe indicates that only one has. For events with both electrons in the CC, it must hold identically that

$$\epsilon^2 + 2\epsilon(1-\epsilon) + (1-\epsilon)^2 \equiv 1,$$

where ϵ is the single track finding efficiency in the CC. The first term is the fraction of events where each electron has a matching track, the second term, where only one electron has a matching track, and the third term, neither. For events with one electron in the CC and one in the EC, it is identically true for the electron in the CC that $\epsilon + (1-\epsilon) \equiv 1$. The efficiency in the CC is found by counting the number of CC-CC events that are ee, $N_{ee,CC-CC}$, and γe, $N_{\gamma e,CC-CC}$, the number of CC-EC events that are ee, $N_{ee,CC-EC}$, and γe, $N_{\gamma e,CC-EC}$. The efficiency for track finding in the CC, ϵ, is given by

$$\frac{\epsilon}{1-\epsilon} = \frac{2N_{ee,CC-CC}}{N_{\gamma e,CC-CC}}$$

using CC-CC events and also by

$$\frac{\epsilon}{1-\epsilon} = \frac{N_{ee,CC-EC}}{N_{\gamma e,CC-EC}}$$

using CC-EC events. The weighted average is taken. The EC electron is required to have a matching track in the second calculation above. Events where neither electron has a matching track are not used since the background contamination is large compared to the number of events. The efficiency in the EC is calculated similarly, substituting EC-EC for CC-CC, etc. The track finding efficiency is:

- CC: 0.853 ± 0.011
- EC: 0.832 ± 0.019.

The combined event reconstruction efficiency from the above sources is:

- CC: 0.744 ± 0.016
- EC: 0.668 ± 0.021.

3.4 QCD background

There are 9135 events remaining in the final $W(W')$ candidate event sample after the foregoing selection criteria are applied. The principal background in this sample arises from QCD multijet events in which one of the jets is misidentified as an isolated electron and there is also mismeasured $\not\!\!E_T$ in the event. The method of determining the QCD background in the W sample may be summarized as follows. An event sample is selected with the same electron selection criteria as the W sample but with $\not\!\!E_T < 20$ GeV. Because of the low $\not\!\!E_T$ requirement, electrons in this sample are primarily background arising from QCD events, not the result of W decay. The cross section for this process is then extrapolated to the region of $\not\!\!E_T > 30$ GeV by studying the $\not\!\!E_T$ distribution of similar QCD events. The amount of this background is 551 ± 96 events.

The summary of the QCD background estimate given in the preceding paragraph is now presented in more detail. The following study applies to an event sample of 9096 events after a cut on the W transverse momentum, $P_T^W < 100$ GeV. This cut removes 38 events that are presumed to be all QCD background but it is not used in the W' search as it is not fully efficient for W'. We start with the W event sample and select events with low

$\not{E}_T$, $\not{E}_T < 15$ GeV. We determine the ratio of good to bad "electrons". Bad "electrons" are defined by anti-electron cuts, $I > 0.1$ and $SIG > 10$ in this study. We also determine the number of bad "electrons" in the sample with $\not{E}_T > 30$ GeV. The fraction of QCD background in the data is then given by:

$$\text{background fraction} = \left(\frac{good}{bad}\right)_{\not{E}_T<15} \left(\frac{bad}{good}\right)_{\not{E}_T>30}.$$

The principal systematic error in this result involves real electrons that would tend to corrupt the numerators of both ratios. This would result in an overestimate of the background. The fractional background is:

$$CC: \quad 3.2 \pm 1.0\% = \frac{179}{21}\frac{24}{6361}$$

$$EC: \quad 10.8 \pm 2.8\% = \frac{710}{53}\frac{22}{2735}.$$

The background to W is computed in this manner in Ref. [32] for tighter cuts, $\chi^2 < 100$, $I < 0.1$, and $SIG < 5$. That study reports: background fraction in the CC, $1.9 \pm 0.3\%$, and EC, $12.0 \pm 0.9\%$. This tighter selection criteria will be referred to as "tight" and the W' electron selection criteria as "loose".

It is useful to demonstrate that background and efficiency estimates describe the data in going from tight to loose cuts. Given tight cuts, there are 6052 CC events in the W sample with a predicted background of 1.9% or 115 events leaving 5937 signal events. These figures may be projected to the loose cuts used in the W' search using the relative increase in efficiency for electron identification, 1/0.975, determined from the Z sample and the relative increase in the fake rate, the probability that a jet will be identified as an electron, determined from dijet events to be 1.76. This projects to 6089 signal, 202 background,

and 6291 total events. There are 6361 events observed. The projected background fraction computed using the projected total events is 3.2%, the same as the background calculation above.

In the EC, there are two factors that might cause the background fraction reported in Ref. [32] to be high relative to this study. First the E_T^e threshold is decreased from 30 to 25 GeV. This causes about a 10% increase in background fraction in the EC. No effect is seen in the CC. Second Ref. [32] includes electrons located in $1.4 < |\eta| < 1.5$ in the EC. Electron identification is not as reliable in this area. Using tight electron identification cuts, fiducial η, and $E_T^e > 30$, the EC background fraction is found to be $5.8 \pm 1.5\%$.

Given tight cuts, there are 2063 W candidates in the EC of which 5.8% or 120 are background and 1943, signal. Projecting to loose cuts, the efficiency factor is 1/0.809 and the relative fake rate is 2.53, which gives 2402 signal, 303 background, and 2705 total. There are 2732 observed events. The projected background fraction is 11.1%, consistent with 10.8%.

With the P_T^W cut removed, the QCD background is calculated:

$$CC: \quad 3.9 \pm 1.0\% = \frac{407}{43}\frac{26}{6389}$$

$$EC: \quad 11.1 \pm 2.7\% = \frac{1074}{81}\frac{23}{2745}.$$

The $\not{E}_T$ constraint on the first fraction is increased from 15 to 20 GeV to improve statistics but the fraction does not change. Of the 9135 W candidates, 6389 are in the CC and 2745, EC. The estimated QCD background is 246 ± 63 events in the CC and 305 ± 73 events, EC.

3.5 W cross section

From the entire preceding set of efficiency studies, only the geometric and kinematic acceptance, and the QCD background estimate are used in the W' analysis. It is a useful exercise though to demonstrate from the cross section calculation that an appropriate data sample has been selected and that the acceptance and background estimates are reasonable. W cross sections may be produced separately for the CC and EC. The τ channel is treated as background. The τ background in W events, determined from the relative acceptances, is 1.9% in the CC and EC. Taking the luminosity as 13.5 pb^{-1} without error since the error is common to both, the cross sections are:

- CC: 2.61 ± 0.11 nb
- EC: 2.56 ± 0.14 nb.

The cross section times branching ratio $\sigma B(W' \to e\nu)$ reported by DØ is 2.38 ± 0.07 nb [33]. The figure that may be inferred from CDF Ref. [34] is 2.52 nb.

3.6 Comparison of the background model to data

Trigger and electron identification efficiencies are different for the CC and EC. Module boundary cuts reduce the fiducial area in the CC as well. This difference was introduced into the W Monte Carlo by giving different weights to events in the CC and EC. Weights are chosen to exactly reproduce the CC/EC event ratio seen in the data after background subtraction. About 6% of the W event sample is expected to be background from QCD events. The model for QCD background is taken from the data, specifically from the bad "electron" events in the QCD background study. Events are selected with the following

anti-electron criteria: $\chi^2 > 50$, SIG > 5, and either I > 0.08 or $1.5 <$ MIPS < 2.5. There are 176 events in the sample which are scaled to represent the 551 QCD background events. The W Monte Carlo is normalized to the the observed events less QCD background. The combined W Monte Carlo plus QCD background is the model of the background for W' and is normalized to the observed events. In the following figures comparing Monte Carlo plus QCD to data, Monte Carlo plus QCD is shown as a histogram and the data as discrete points. Figure 3.1 shows the electron transverse energy, Fig. 3.2 shows the electron pseudorapidity distribution, and Fig. 3.3 depicts the missing transverse energy distribution. The agreement between data and the simulation is reasonably good. The transverse energy of the most energetic hadronic jet is shown in Fig. 3.4. For about 90% of the signal, the agreement is quite good. There are 2570 events in the data and 2320 in the model. All of the difference is for $E_T > 25$ GeV. We are only interested in modeling the jet response to get the $\not\!\!E_T$ resolution modeled correctly and this has been accomplished. PYTHIA is not expected to model the $W+1$ jet production exactly. Figure 3.5 shows the pseudorapidity distribution for the most energetic jet. The agreement is good except in the range $|\eta| = 1.1 - 1.5$, the IC region. The rabbit-ear shape of the data distribution is believed to be due to the poor energy resolution in the IC. The W Monte Carlo used a $120\%/\sqrt{E}$ resolution for the IC, however the pseudorapidity distribution is not quite properly described. Figure 3.6 shows the transverse momentum, $p_T^{e\nu}$, for the W candidates compared to W Monte Carlo plus QCD. For $p_T > 60$ GeV there are 150 events in the data and 70 in the background model. This disagreement could be caused by inaccurate modeling of the background due to the limited size of the QCD background sample, higher order corrections not included in PYTHIA, or additional $\not\!\!E_T$ resolution effects not included in the detector simulation.

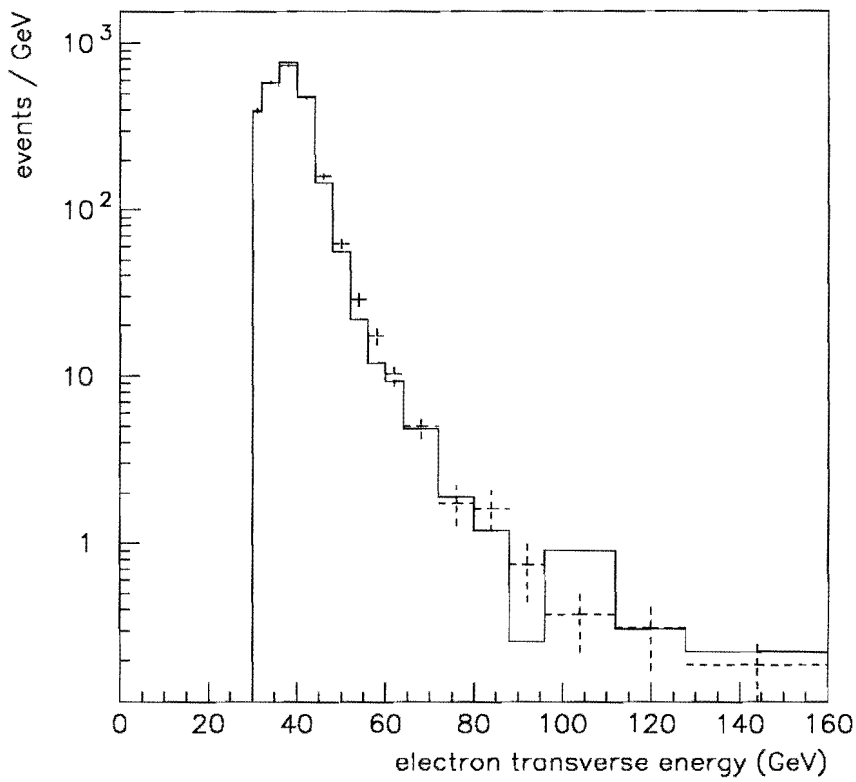

FIG. 3.1: The electron E_T for data (discrete points) and W Monte Carlo plus QCD.

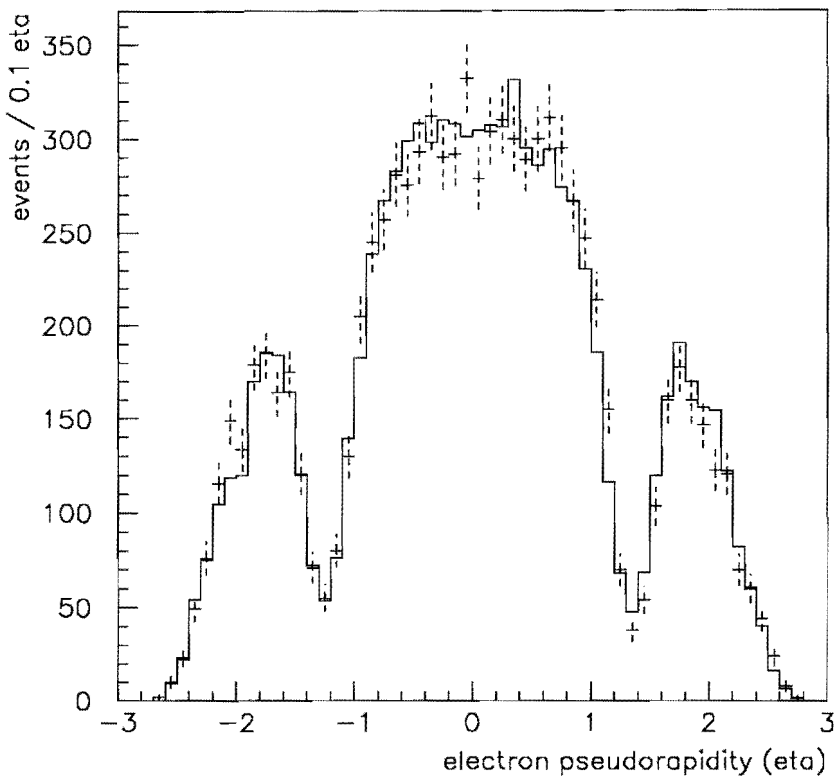

FIG. 3.2: Electron η for data (discrete points) and W Monte Carlo plus QCD.

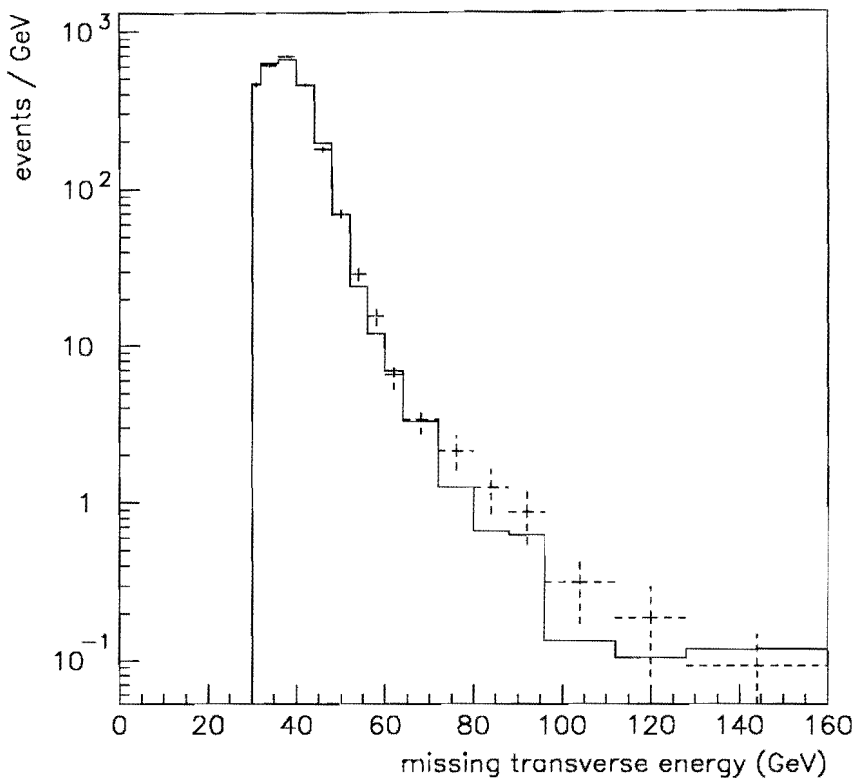

FIG. 3.3: The $\not\!\!E_T$ for data (discrete points) and W Monte Carlo plus QCD.

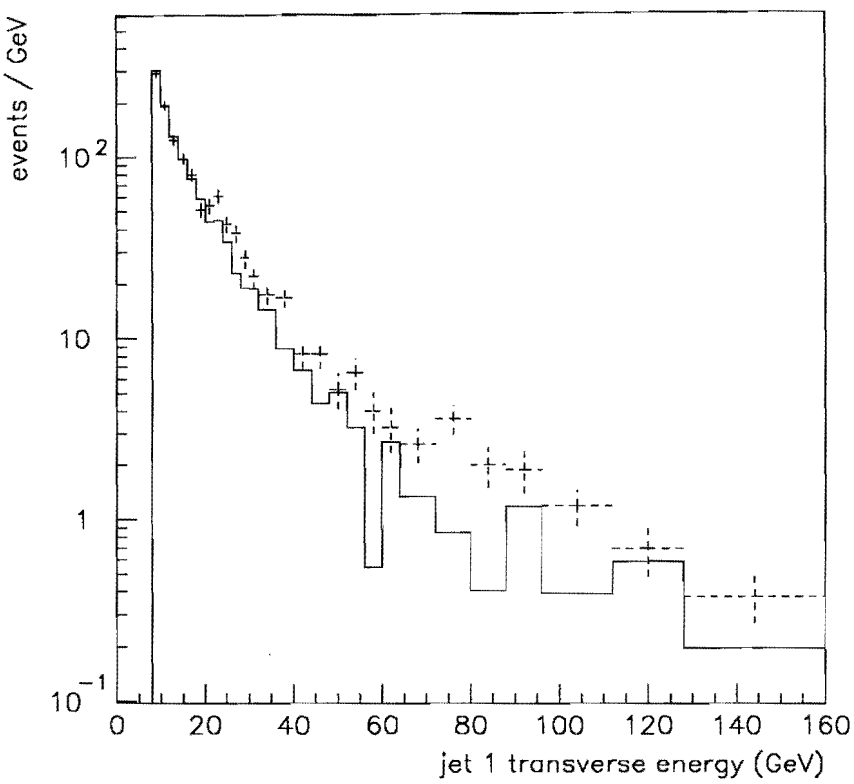

FIG. 3.4: The E_T of the leading hadronic jet for data (discrete points) and W Monte Carlo plus QCD.

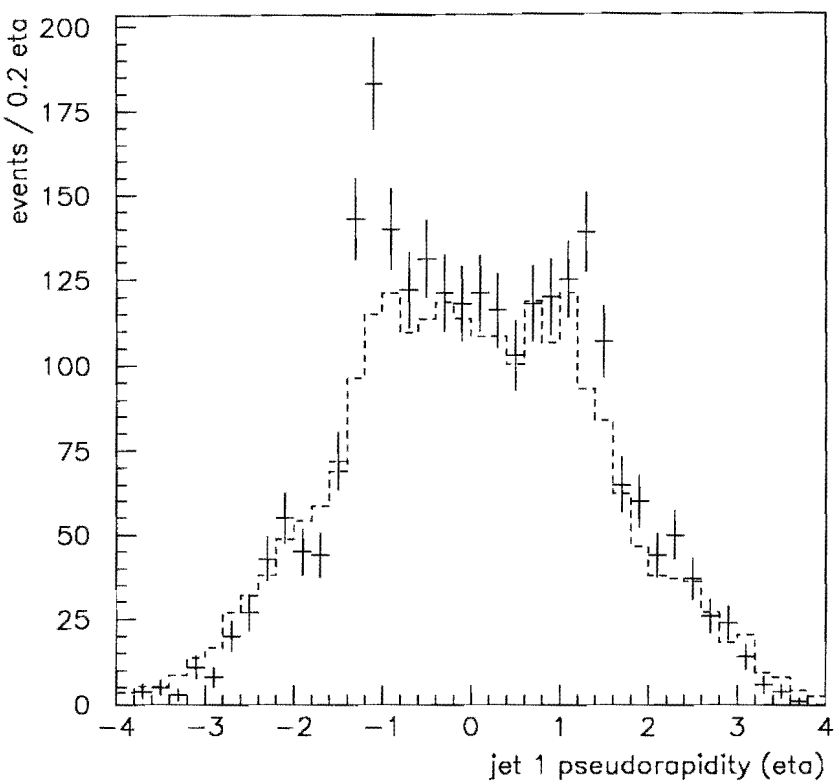

FIG. 3.5: The η of the leading jet for data (discrete points) and W Monte Carlo plus QCD.

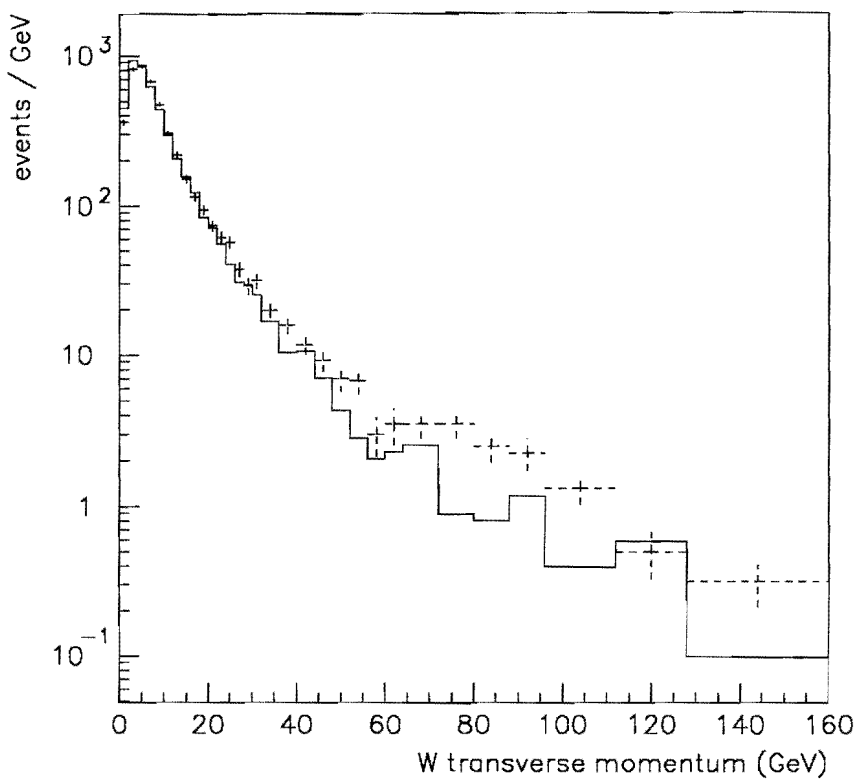

FIG. 3.6: The W P_T for data (discrete points) and W Monte Carlo plus QCD.

It is important to model the $m_T^{e\nu}$ spectrum of the background accurately to perform a credible search for W'. The $m_T^{e\nu}$ distribution of the QCD background is taken from the data, specifically from the bad "electron" events in the QCD background study. To smooth the distribution, the available data is fitted with an exponential for $m_T^{e\nu} > 60$ GeV. The exponential is normalized to the expected QCD background and added to the W Monte Carlo. Figure 3.7 shows the transverse mass, $m_T^{e\nu}$, distribution for data and W Monte Carlo plus QCD background modeled from data. The simulation plus QCD reproduces the data well. In the region $m_T^{e\nu} > 250$ GeV, there are 3 events in the data sample. Monte Carlo plus QCD predict 1.3 ± 0.4 events. In the region $m_T^{e\nu} > 150$ GeV, there are 16 events in the data sample. Monte Carlo plus QCD predict 19.4 ± 5.7 events.

A visual scanning of the 26 events with $m_T^{e\nu} > 130$ GeV reveals that three events are clearly the result of bremsstrahlung from cosmic muons [35]. The transverse masses of the three events are 133, 244, and 361 GeV. The 361 GeV event is the highest transverse mass in the sample. The next highest event is 304 GeV. No method was found to eliminate these events based on information contained in the event (DST). These events frequently do not contain reconstructed muons since the muon is not in time with the beam crossing and does not approach r=0 very closely. The events are left in the analysis. Doing so lowered the mass limit from 620 Gev to 610 GeV.

3.7 W' Monte Carlo

To determine the acceptance for W', samples of W' were generated for $m_{W'}$ equal to 100 to 800 GeV. Again PYTHIA 5.7, MRS D$-'$ pdf's, and the fast detector simulator were used. The W' width $\Gamma_{W'}$ was assumed to scale with the W' mass, $\Gamma_{W'} = (m_{W'}/m_W)\Gamma_W$.

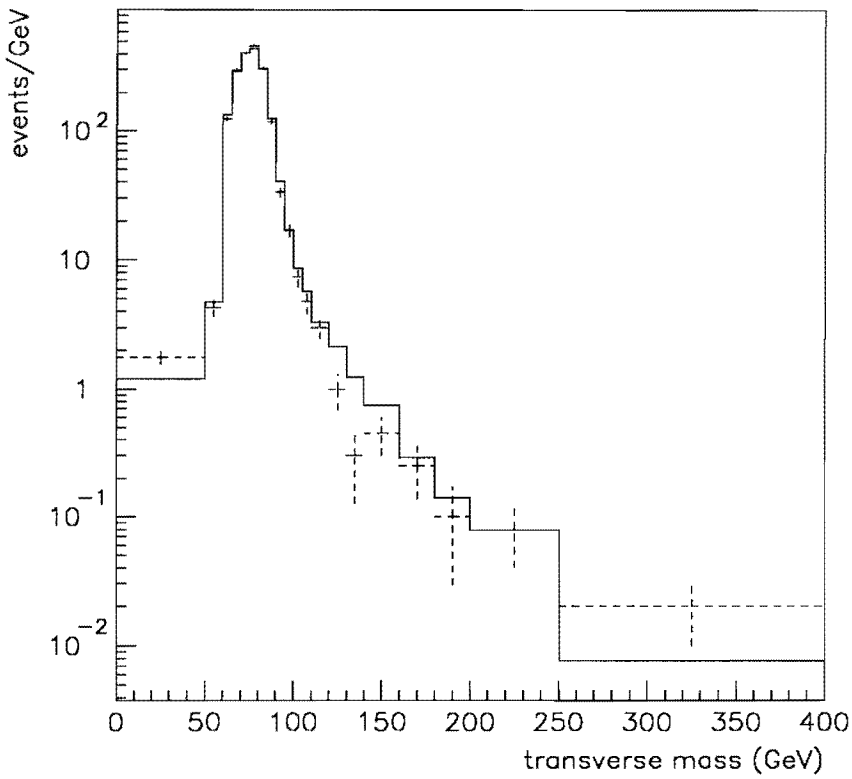

FIG. 3.7: Electron-neutrino transverse mass distribution for data compared to W Monte Carlo plus QCD background.

$m_{W'}$ (GeV)	$A_{W'}/A_W$	$m_T^{e\nu}$ min., fit region	observed events	expected background	95% CL, $N_{95}^{W'}$	95% CL, $\sigma B_{W'}/\sigma B_W$ ($\times 10^{-4}$)
100	1.48	80	2509	2620 ± 86	36.3	39.4
200	2.19	140	23	28.8 ± 7.2	12.4	10.2
300	2.46	210	7	4.3 ± 0.8	7.8	6.2
400	2.51	270	3	0.9 ± 0.3	6.2	4.7
500	2.54	330	1	0.2 ± 0.1	4.4	3.3
600	2.54	380	0	< 0.1	3.0	2.3
700	2.48	380	0	< 0.1	3.0	2.3
800	2.41	380	0	< 0.1	3.0	2.5

TABLE 3.2: For each W' mass: W' acceptance relative to W, minimum $m_T^{e\nu}$ of the fit region, the 95% CL expressed as expected events, and the 95% CL expressed as $\sigma B(W' \to e\nu)/\sigma B(W \to e\nu)$.

For $m_{W'} \geq 200$ GeV, $\Gamma_{W'}$ is scaled by an additional factor of $\approx 4/3$ since decay channels involving the top quark are assumed to be available. However the impact of the actual value of $\Gamma_{W'}$ on the experimental signature, within the theoretically expected range of $\Gamma_{W'}$, is negligible. This is due to the fact that the observed variable, transverse mass, has a much broader distribution than the mass.

The W' detection efficiency with respect to the W, $A_{W'}/A_W$, was evaluated as a function of $m_{W'}$. In this calculation, trigger and electron reconstruction efficiencies were assumed to be constant with electron energy. This is substantiated by data from test beam electrons up to 150 GeV and by studying high energy electrons in a full detector simulation. Therefore the ratios obtained reflect the difference in geometrical and kinematic acceptance. The relative W' efficiencies are shown in Table 3.2. The systematic uncertainty in this ratio due to choice of pdf's is estimated to be 2%. The relative W' to W geometrical and

kinematical acceptance calculated with PYTHIA and DYRAD [36] were compared. The relative difference, 1%, was taken as an estimation of the systematic error due to radiative corrections. The uncertainty in the measurement of $\not{E}_T$ was estimated by varying the hadronic energy degradation used in the Monte Carlo simulation by $\pm 5\%$. The systematic error due to this effect was estimated to be 1%. There is also a 1% uncertainty due to Monte Carlo statistical precision giving a total uncertainty in $A_{W'}/A_W$ of 3%.

3.8 Extracting a limit

A binned likelihood approach with Poisson statistics was applied to the transverse mass distribution in order to obtain an upper limit on the process $p\bar{p} \rightarrow W' \rightarrow e\nu$. The probability that n_i events will be experimentally observed in the ith bin is given by:

$$P_i = \frac{(f_i)^{n_i} e^{-f_i}}{n_i!}$$

where f_i is the number of predicted events. The function f_i is given by:

$$f_i = (1-\alpha) f_i^B + \alpha f_i^{W'}$$

where f_i^B is the W plus QCD background, $f_i^{W'}$ is the W' signal, and α is a free parameter that is varied from 0 to 1. The functions f_i^B and $f_i^{W'}$ are each normalized to the number of events in the sample,

$$\sum_i^N f_i^B = \sum_i^N f_i^{W'} = N_{\text{obs}},$$

where N_{obs} is the number of W candidates observed experimentally. Therefore f_i is also normalized to the observed data.

The total probability P is given by

$$P = \prod_{i=1}^{N} \frac{(f_i)^{n_i}}{n_i!} e^{-f_i}.$$

Written as a function of α, P becomes a probability density function, $P(\alpha)$ that is normalized to 1 by integrating over α.

In this analysis the W contribution is much larger than that expected from W', especially at low m_T. This difference increases as the W' mass grows. In order to avoid fitting over regions that are dominated by background, only those bins where the W' contribution is significant were considered. The expected W' signal is partitioned into 10 bins by $m_T^{e\nu}$, each containing $\approx$ one tenth of the expected signal. The top 6 bins, $\approx 60\%$ of the signal, are included in the fit.

The purpose of this analysis is to set an upper limit on W' production. This corresponds to establishing the minimum value of α (least upper bound) compatible with the experimentally observed event distribution at a certain confidence level (CL). The 95% CL limit on the α parameter, α_{95}, is obtained numerically from:

$$0.95 = \frac{\int_0^{\alpha_{95}} P(\alpha) d\alpha}{\int_0^1 P(\alpha) d\alpha}.$$

The parameter α times the normalization of $f_i^{W'}$ gives the number of expected W' events, $N_{W'}$, for a given α: $N_{W'} = \alpha \times N_{\text{obs}}$. (This would be true regardless of the normalization chosen for $f_i^{W'}$ and would also be true in a two-parameter fit.) The physical observable being varied when α is varied is $N_{W'}$. Therefore, this procedure determines the 95% CL limit for $N_{W'}$,

$$N_{95}^{W'} = \alpha_{95} \times N_{\text{obs}},$$

where $N_{95}^{W'}$ is the limit on expected W' events. The limit $N_{95}^{W'}$ may be expressed as a 95% CL limit on $\sigma B(W' \to e\nu)/\sigma B(W \to e\nu)$ using

$$\left(\frac{\sigma B_{W'\to e\nu}}{\sigma B_{W\to e\nu}}\right)_{95} = \frac{A_W}{A_{W'} A_f N_W} N_{95}^{W'},$$

where N_W is $N_{\rm obs}$ less QCD background and A_f is the fraction of the W' acceptance included in the fit. A_f is typically $\approx 60\%$.

The uncertainty in the scale factor, $A_W/(A_{W'} A_f N_W)$, may be transferred to $N_{W'}$ and included as an uncertainty in the probability distribution, $P(\alpha)$. This uncertainty consists of the systematic error on $A_{W'}/A_W$ described in 3.7 and the statistical error on N_W, $\pm 1.6\%$. This is combined to give a total error of 4%. This error, ε, can be incorporated into the probability distribution by assuming a Gaussian distribution, $G(\varepsilon)$, and convoluting the functions:

$$P'(\alpha) = \int_{-\infty}^{\infty} P(\alpha, \varepsilon) G(\varepsilon) d\varepsilon.$$

There is also uncertainty in $P(\alpha)$ due to the overall normalization of the background in the fit region. The full background sample is normalized to the number of observed events. However only the high transverse mass tail of the background is used in the fit and that region is not independently normalized to the data. The uncertainty arises from the statistical uncertainty in the W Monte Carlo, the uncertainty in the choice of pdf's, and the uncertainty in the shape and magnitude of the QCD background. The background and uncertainty included in the fit region are shown in Table 3.2. The error on the background may be incorporated in the $P(\alpha)$ distribution by adding a second integral:

$$P'(\alpha) = \int_{-\infty}^{\infty} \int_{-\infty}^{\infty} P(\alpha, \varepsilon, \varepsilon') G(\varepsilon) G(\varepsilon') d\varepsilon d\varepsilon'.$$

The 95% CL limit on $\sigma B(W' \rightarrow e\nu)/\sigma B(W \rightarrow e\nu)$ is obtained as described above substituting $P'(\alpha)$ for $P(\alpha)$. Table 3.2 gives the 95% CL limit on this ratio, the limit expressed as expected events, the observed events, and the range of the fit for the different W' masses considered. The 95% CL upper limit on $\sigma B(W' \rightarrow e\nu)/\sigma B(W \rightarrow e\nu)$ is plotted as a function of the $m_{W'}$ in Fig. 3.8 together with the theory curve, the value of this ratio assuming SM couplings. The theory curve was determined using Born level cross sections and second order K factors [37]. In detail, the K factor is computed as a function of Q^2, the invariant mass of the $e\nu$ pair. The Born level invariant mass distributions from PYTHIA for $m_{W'} = 100$ to 800 GeV are scaled event by event with the appropriate K factor. The average scaling factor for each $m_{W'}$ is the effective second order K factor as a function of $m_{W'}$. There is an uncertainty in the theory of 3% due to choice of pdf's. As determined by the intersection of the two curves, a W' with the same couplings to quarks and leptons as the standard model W is excluded at the 95% CL for $m_{W'} < 610$ GeV with the assumption that the neutrinos produced in the W' decay are stable.

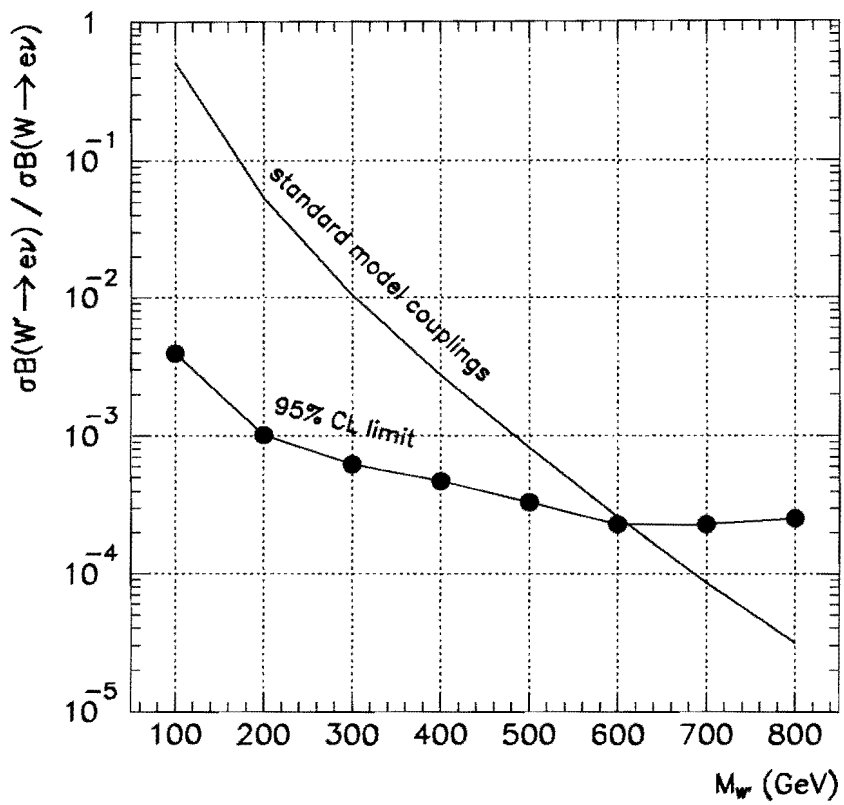

FIG. 3.8: 95% CL upper limit as a function of $m_{W'}$ for $\sigma B(W' \to e\nu)/\sigma B(W \to e\nu)$. The expected value using standard model coupling is also shown.

Chapter 4

Z' search

4.1 Data sample

The event sample for the Z' search is selected from the full run 1a data set. The data was processed by the event reconstruction program, DØRECO versions 11.17, 11.18, and 11.19. The luminosity for this sample for the trigger used in this analysis, ELE_2_MAX, is 14.5 pb^{-1}. The luminosity is about 7% greater than for the W sample since data was taken during certain noisy parts of the Main Ring cycle. The Main Ring passes through the hadronic section of the DØ calorimeter and can deposit energy in the neighboring calorimeter cells. This degrades the $\not\!\!E_T$ resolution but does not affect the Z sample. The electron energies were corrected as in the W analysis, using the Z boson mass for calibration. The $\not\!\!E_T$ was also corrected but only to observe that the $\not\!\!E_T$ distribution was as expected. No cut was made on $\not\!\!E_T$.

4.2 Event selection

The following criteria are used to select $Z(Z')$ candidates. The level 2 trigger ELE_2_MAX is required. ELE_2_MAX is defined as follows. In the associated level 1 trigger, events are required to have two electromagnetic trigger towers of size 0.2×0.2 ($\Delta\eta \times \Delta\phi$) with $E_T > 7$ GeV. In level 2, two clusters with $E_T > 20$ GeV fulfilling isolation and electromagnetic shape criteria are required.

After event reconstruction, candidate events are required to have two electromagnetic clusters with transverse energy $E_T^e > 30$ GeV. This value is chosen to be safely above the

trigger threshold but to retain substantial Z signal and be nearly fully efficient for Z'.

In the following discussion of electron identification requirements, we refer to the two EM objects as electrons even though they can in fact can be fake electron background or photons. We only require a matching track for one of the electrons. The definitions of the electron identification variables are the same as in the W analysis. The following electron identification requirements are applied to select $Z(Z')$ candidates. The cuts are required for both electrons in the event unless noted. Again the cuts are kept loose to keep selection efficiency relatively high. The cuts are loosened to the point where in the region $m_{ee} > 150$ GeV the signal/background ratio is $\approx 1:1$ for $Z\gamma^*$ signal and QCD background. (m_{ee} is the invariant mass of the electron pair. $Z\gamma^*$ is Z + Drell-Yan production. QCD background is discussed in 4.3.)

- Isolation < 0.15.
- Electromagnetic fraction > 0.9.
- H-matrix $\chi^2 < 200$.
- Track matching significance, SIG$<$ 5 for at least one of the electrons. There is no requirement on the other electron. So as noted, only one of the electrons is required to have a matching track.

In subsequent discussion of electron selection efficiencies and QCD fake electron rates, the electron identification requirements with SIG $<$ 5 are called "tight" and those without a track requirement are called "loose".

Electrons are also required to be in the fiducial region of the calorimeter. For the CC, the requirement is $|\eta| < 1.1$. In addition, shower centers must be > 0.01 radians from ϕ

module boundaries. In the EC the fiducial region is $1.5 < |\eta| < 2.5$. It is further required that the z coordinate of the primary vertex be within 100 cm of $z = 0$.

There is also a topological cut applied to $Z(Z')$ candidate events. At least one electron must be in the CC. Events with both electrons in the EC are not accepted. For $m_{Z'} >$ 150 GeV, almost all rejected events would have one electron in EC north and one in EC south. This forward-backward topology is common in QCD dijet events which form the fake electron background. The estimated QCD background for this topology would exceed the expected Z' signal so this topology is eliminated. For $m_{Z'} = 500$ GeV, the acceptance for a Z' is reduced by $\approx 7\%$.

4.3 QCD background

The principal background in the $Z(Z')$ sample is QCD multi-jet events in which jets are reconstructed as isolated electrons. Fake electrons can arise from jets in which a π^0 carrying most of the jet energy overlaps with a charged particle, from the charge exchange interaction of charged pions near the surface of the EM calorimeter, and from converted photons, principally from π^0 decay. In addition heavy quark decays could produce isolated real electrons which are considered fake for the purpose of this study since they do not arise from Z decay. The amount of this background is determined from the data.

A summary of the procedure to determine the QCD background in the $Z(Z')$ sample follows. Events are selected with one "good" electron and one jet, each with $E_T > 30$ GeV. No effort is made to remove real W's and Z's from this sample and their contribution is estimated to be 2.3%. The fake cross section obtained from this sample is divided by the exclusive dijet cross section for jets with $E_T > 30$ GeV to get a fake rate. The $rate^2 \times$

$\sigma_{inclusive\ dijet} \times$ *integrated luminosity* gives the predicted number of fake di-electrons in the Z sample, 38 ± 3. Appropriate allowances are made for the the fact that there are two types of electron identification, tight and loose, and different fake probabilities in the CC and EC. Note that the large systematic errors in luminosity used in this calculation cancel since only DØ measured cross sections are used.

The luminosities used in this study reflect the original luminosity scale used by DØ prior to July 1994. At that time, luminosities were rescaled $\approx -10\%$ to reflect a new determination of the inelastic cross section. The background estimate is independent of luminosity scale.

In more detail, there are two principal data sets used in this study. The first set is the fake sample. It is selected from the full run 1a data set (ALL stream), DØRECO version 11.19, runs 62158-63095. The trigger ELE_HIGH is required. This trigger requires the same electron quality for a single electron as the trigger used for the Z sample requires for both. The luminosity for the sample is found to be 2.67 pb-1 using the luminosity utility. This value can be double checked by using the ratio of the number of W candidates in this sample to the number in the full data set:

$$\frac{2244}{12714} \times 15.1 \text{ pb}^{-1} = 2.67 \text{ pb}^{-1}.$$

The first event sample, referred to as the *fake* sample, consists of dijet events, $p\bar{p} \rightarrow jjX$, in which at least one of the two leading jets has an associated electron. An electron is associated with the jet if the distance from the electron to the center of the jet is less than 0.1 in η, ϕ coordinates. Jets are defined within a cone, $R = 0.5$. The jet energy, electron energy, and $\not{E}_T$ are corrected as described for the W sample. The electron must be in the

same fiducial area as in the Z sample. The z coordinate of the vertex must be within 100 cm of $z = 0$. The other of the two leading jets, referred to as the jet, must be a good jet. The following cuts are applied to eliminate jets arising from noise: CH fraction< 0.4, $0.05 <$ EM fraction < 0.95, and HOT fraction < 10. HOT fraction refers to the the ratio of the energy of the leading cell to the next-to-leading cell in the jet. The detector η of the center of the jet must lie within the fiducial η for electrons. Given an E_T threshold, for example 30 GeV, and a set of electron identification criteria, a cross section may be determined, σ_{ej}, where both the electron e and jet j are above the threshold.

The second event sample, referred to as the *dijet* sample, is selected from QCD DST's. The events are selected from the run range corresponding to trigger menus version 7.3 and 7.4, runs 64086-65429. The trigger JET_MIN is required. The trigger requires at least one jet, $R = 0.3$, with $E_T > 15$ GeV. The trigger is taken to be efficient, efficiency > 0.9, for events with two jets, $R = 0.5$, $E_T > 30$ GeV. There are three arguments for this assumption. First, trigger turn on curves for a jet trigger with a threshold of 20 GeV show it to be $> 90\%$ efficient for two jets > 35 GeV. Second, the ratio of the cross section for two jets > 25 GeV to two jets > 30 GeV is 2.0 in the data and the same in PYTHIA. Finally, the fake rates determined with E_T thresholds of 25 and 30 GeV are substantially the same. If the trigger were inefficient for two jets > 25 GeV, the fake rate should have increased.

The luminosity for the dijet sample as determined by the QCD luminosity program, LUMIN_SP, is 1.91 nb. The luminosity determined by the luminosity utilities is $\approx 5\%$ greater. The detector η of the center of both jets must be within the fiducial η for electrons. Additionally both jets must satisfy EM fraction > 0.05 and CH fraction < 0.4. Given an E_T threshold, for example 30 GeV, a cross section may be determined, σ_{jj}, where both

jets are above the threshold. The fake rate is σ_{ej}/σ_{jj}. To predict the background in the dielectron sample:

$$(\frac{\sigma_{ej}}{\sigma_{jj}})^2 \times \sigma_{jj} \times L_{sample} = N_{fakes},$$

where L_{sample} is the luminosity of the dielectron sample (16.2 pb-1) and N_{fakes} is the predicted fake electron background arising in this sample from QCD processes. Since $\sigma = N/L$, this reduces to:

$$\frac{N_{ej}^2}{N_{jj}} \times \frac{L_{jj} \times L_{sample}}{L_{ej}^2} = N_{fakes}.$$

Since only DØ determined cross sections are used, the large systematic uncertainties in L cancel. The error on N_{fakes} is the statistical error on N_{ej}^2/N_{jj} which is typically $\approx 6\%$ and the uncertainty in the jet energy scale. This uncertainty can be limited as will be shown later.

One can impose an invariant mass constraint on the ej pair in σ_{ej} and on the jj pair in σ_{jj} and calculate fake rates for specific invariant mass ranges in the dielectron spectrum. This has been done for tight, loose, and standard electron identification criteria. Standard criteria are those used in W' analysis. The results in all cases are consistent with no invariant mass dependence in the fake rates. The fake rates for two invariant mass ranges with standard electron identification are:

$$\begin{array}{llll} m_Z \pm 20 & CC: & 4.3 \times 10^{-4} & EC: \quad 13.3 \times 10^{-4} \\ m_{ee} > 125 & CC: & 4.7 \times 10^{-4} & EC: \quad 12.7 \times 10^{-4}. \end{array}$$

There are two small corrections to the fake rate, in particular, to σ_{ej}. First there is real electron background in the fake sample arising from W and Z events. The amount of this background is estimated from the respective event samples to be $2.3 \pm 0.2\%$ given standard cuts. Second, tighter jet quality cuts were imposed on the fake sample than on

the dijet sample. The dijet sample did not have the cuts: EM fraction < 0.95 and HOT fraction < 10. The cross section σ_{ej} should be increased to reflect the fact that the quality cuts on the jet in that sample are tighter. The amount of this correction as determined from the dijet sample is $1.5 \pm 0.2\%$. The net effect of both corrections is $-0.8 \pm 0.3\%$. No correction is made. The jet quality cuts imposed on the dijet sample are $\approx 100\%$ efficient for jets associated with real electrons as determined from the $W + 0$ jets sample.

The calculation of the QCD background in the dielectron sample with the E_T threshold at 30 GeV and one tight and one loose electron proceeds as follows. The cross sections by event topology for the two leading jets above threshold are:

$$\begin{array}{lll} \sigma_{jj,\ CC-CC}: & (1101 \text{ events}) & 578 \text{ nb} \\ \sigma_{jj,\ CC-EC}: & (1137 \text{ events}) & 597 \text{ nb} \\ \sigma_{jj,\ EC-EC}: & (201 \text{ events}) & 106 \text{ nb.} \end{array}$$

The cross sections by electron location for fake tight electrons and fake rates are:

$$\begin{array}{llll} \sigma_{ej,\ CC} & (1838 \text{ events}) & 689 \text{ pb} & \text{fake rate}: \ 3.9 \times 10^{-4} \\ \sigma_{ej,\ EC} & (1829 \text{ events}) & 685 \text{ pb} & \text{fake rate}: \ 8.5 \times 10^{-4}, \end{array}$$

and for loose cuts are:

$$\begin{array}{llll} \sigma_{ej,\ CC} & (8466 \text{ events}) & 3.17 \text{ nb} & \text{fake rate}: \ 18.1 \times 10^{-4} \\ \sigma_{ej,\ EC} & (5357 \text{ events}) & 2.01 \text{ nb} & \text{fake rate}: \ 24.9 \times 10^{-4}, \end{array}$$

where, for example, the fake rate for CC is given by:

$$\frac{\sigma_{ej,\ CC}}{2 \times \sigma_{jj,\ CC-CC} + \sigma_{jj,\ CC-EC}}.$$

The denominator includes both dijet topologies that can produce an electron in the CC. The factor of 2 occurs since either jet in the CC-CC topology can produce the electron.

The fake rate was determined using σ_{jj} for the two leading jets. To determine the expected fake background, we need to use a probability weighted cross section, $\sigma_{jj,\ P}$, that

weights events by the number of dijet pairs above threshold. In practice, it is sufficient to look at the three pairs that may be constructed with the three leading jets. The cross sections by event topology for dijet pairs above threshold from the three leading jets are:

$$\begin{array}{lll} \sigma_{jj,\ P,\ CC-CC} & (1101 + 59 + 50 \text{ events}) & 635 \text{ nb} \\ \sigma_{jj,\ P,\ CC-EC} & (1137 + 37 + 34 \text{ events}) & 634 \text{ nb.} \end{array}$$

We can now calculate the expected background using

$$(\text{fake rate})^2 \times \sigma_{\text{jj, P}} \times \text{L}_{\text{sample}} = \text{N}_{\text{fakes}},$$

making allowance for the fact that the tight electron sample is a subset of the loose:

CC-CC:

$$(2 \times 3.9 \times 18.1 - 3.9^2) \times 10^{-8} \times 635 \text{ nb} \times 16.2 \times 10^3 \text{ nb}^{-1} \quad = \quad 13.0$$

CC-EC:

$$(3.9 \times 24.9 + 8.5 \times 18.1 - 3.9 \times 18.5) \times 10^{-8} \times 634 \text{ nb} \times 16.2 \times 10^3 \text{ nb}^{-1} \quad = \quad 22.4.$$

(The luminosity for the event sample before the scale was changed was 16.2 pb^{-1}.) There is a total predicted background in the dielectron sample of 35.4 events.

It is in fact possible to calculate this background correctly without using any jet energy correction. All that is required is to choose a jet threshold sufficiently below the electron threshold so that all electrons in the Z sample would be included in this sample. Once this is assured, the electron E_T becomes just another characteristic of the electrons like for example isolation. One could calculate the dijet background in a dielectron sample with $E_T > 50$ GeV using a dijet sample with $E_T > 25$.

For this analysis it is determined from the $W + 0$ jets sample that for electrons with $E_T > 30$ GeV, the associated electron jets all have $E_{T,\ \text{uncorrected}} > 27$ GeV. The fake

background is calculated as before, but using jets with $E_{T,\ \mathrm{uncorrected}} > 27$ GeV. The cross sections by event topology for the two leading jets above threshold are:

$$\begin{array}{lll} \sigma_{jj,\ CC-CC} & (740 \text{ events}) & 388 \text{ nb} \\ \sigma_{jj,\ CC-EC} & (721 \text{ events}) & 378 \text{ nb} \\ \sigma_{jj,\ EC-EC} & (118 \text{ events}) & 62 \text{ nb.} \end{array}$$

The cross sections by electron location for fake tight electrons and fake rates are:

$$\begin{array}{llll} \sigma_{ej,\ CC} & (1582 \text{ events}) & 593 \text{ pb} & \text{fake rate}: \quad 5.1 \times 10^{-4} \\ \sigma_{ej,\ EC} & (1493 \text{ events}) & 559 \text{ pb} & \text{fake rate}: \quad 11.1 \times 10^{-4}, \end{array}$$

and for loose cuts are:

$$\begin{array}{llll} \sigma_{ej,\ CC} & (7192 \text{ events}) & 2.70 \text{ nb} & \text{fake rate}: \quad 23.3 \times 10^{-4} \\ \sigma_{ej,\ EC} & (5357 \text{ events}) & 1.64 \text{ nb} & \text{fake rate}: \quad 32.7 \times 10^{-4}. \end{array}$$

The cross sections by event topology for dijet pairs above threshold from the three leading jets are:

$$\begin{array}{lll} \sigma_{jj,\ P,\ CC-CC} & (740 + 34 + 32 \text{ events}) & 423 \text{ nb} \\ \sigma_{jj,\ P,\ CC-EC} & (721 + 21 + 18 \text{ events}) & 399 \text{ nb.} \end{array}$$

We can now calculate the expected background using

$$(\text{fake rate})^2 \times \sigma_{\mathrm{jj,\ P}} \times \mathrm{L_{sample}} = \mathrm{N_{fakes}}:$$

CC-CC:

$$(2 \times 5.1 \times 23.3 - 5.1^2) \times 10^{-8} \times 423 \text{ nb} \times 16.2 \times 10^3 \text{ nb}^{-1} \quad = \quad 14.5$$

CC-EC:

$$(5.1 \times 32.7 + 11.1 \times 23.3 - 5.1 \times 11.1) \times 10^{-8} \times 399 \text{ nb} \times 16.2 \times 10^3 \text{ nb}^{-1} \quad = \quad 23.8.$$

There is a total predicted background in the dielectron sample of 38.3 events compared to 35.4 events when a jet threshold of 30 GeV, corrected, was used. The second calculation

should in principle be the most accurate since it is independent of jet energy. The QCD background is taken to be 38.3 ± 2.9 events where the uncertainty 2.9 is the difference between the two calculations. The statistical error is 2.0 events.

To get the distribution of this background, the inclusive dijet invariant mass spectrum is normalized to 38.3 events. Varying the jet energy by $\pm 2\times$ the jet energy scale uncertainty does not noticeably affect this spectrum. To smooth this distribution above 130 GeV where the number of events becomes small, the distribution is fitted with an exponential.

4.4 Comparison of Monte Carlo to data

The principal physics background to the Z' is Z–Drell-Yan production. $Z\gamma^*$ production is modeled using Pythia, version 5.7, with MRS D$-'$ parton distribution functions. The processes are

$$q\bar{q} \rightarrow Z \rightarrow ee \quad + \quad q\bar{q} \rightarrow \gamma^* \rightarrow ee.$$

The interference between these two processes is included in the Monte Carlo. The Monte Carlo output is smeared for detector energy and angular resolution. The energy and angular resolution used are shown in Table 3.1. Trigger and electron identification efficiencies are different for the CC and EC. Module boundary cuts reduce the fiducial area in the CC as well. This difference was introduced into the Monte Carlo by giving different weights to events which are CC-CC and CC-EC by randomly removing 7.0% of the CC-CC events. This weighting is chosen to exactly reproduce the CC-CC/CC-EC ratio seen in the data after background subtraction. The number of simulated events is normalized to the observed data less QCD background. The smeared Z–Drell-Yan invariant mass spectrum and the QCD background invariant mass spectrum are shown in Fig. 4.1. The dielectron invariant

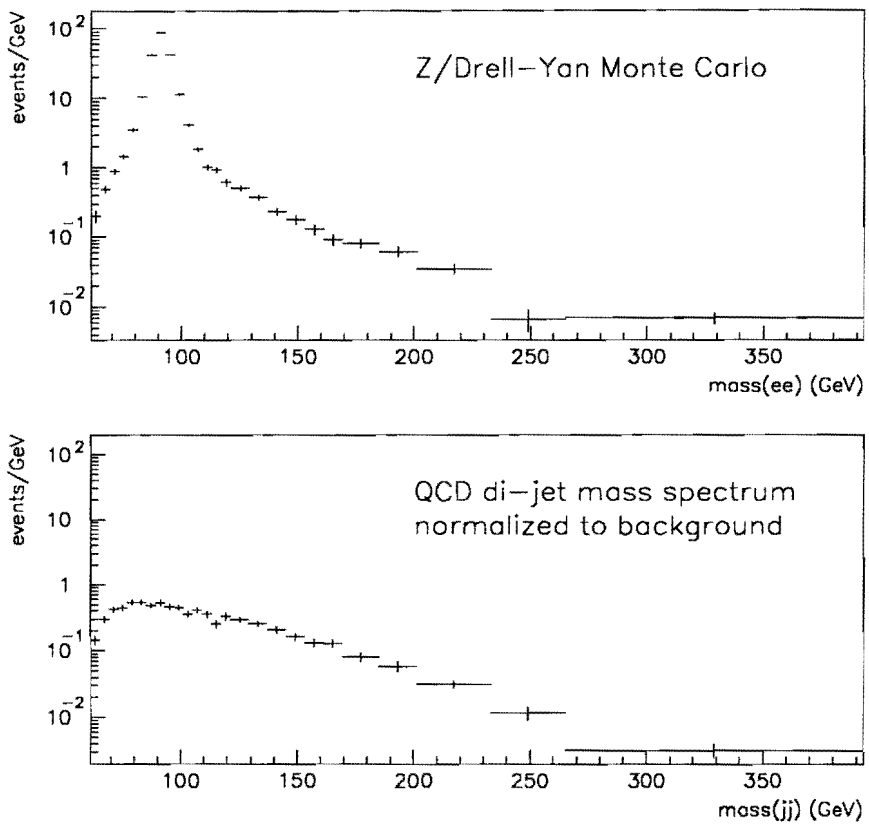

FIG. 4.1: The Z–Drell-Yan and QCD backgrounds to Z'.

mass spectrum from data is compared to the sum of $Z\gamma^*$ Monte Carlo plus QCD background spectra, in Fig. 4.2. The agreement is quite good. To first order based on a visual comparison, no evidence of a Z' signal is seen. In the absence of Z', for $M_{ee} > 200$ GeV we expect 4.2 ± 0.3 $Z\gamma^*$ plus QCD background events. Six events are observed in the data.

4.5 Z' Monte Carlo

A combined Z', Z, and Drell-Yan signal, $Z'Z\gamma^*$, is also modeled by Monte Carlo. Again PYTHIA 5.7, MRS D$-'$ pdf's, and parameterized detector resolutions were used. All of the interference terms are included. Because of the interference effects, it is not possible to generate a Z' signal independently. The difference between $Z'Z\gamma^*$ and $Z\gamma^*$ is the Z' signal. Z' samples were generated for $m_{Z'} = 100$ to 600 GeV. Because the interference term is negative below the Z' pole, the expected Z' signal becomes negative for $m_{ee} < 0.85 m_{Z'}$.

The Z' width $\Gamma_{Z'}$ was assumed to scale with the Z' mass, $\Gamma_{Z'} = (m_{Z'}/m_Z)\Gamma_Z$. For $m_{Z'} \geq 400$ GeV, decay channels involving the top quark are assumed to be available. This scaling is what would be expected in a reference model Z'. It is a conservative assumption since in most Z' models, the Z' width would be smaller than this [38].

The kinematic and fiducial acceptance for the Z' is taken from the Monte Carlo. The trigger and reconstruction efficiencies are assumed to be the same for Z''s as for the Z. Since the Z' limit is calculated in the same manner as the W', only the uncertainty in the ratio of the kinematic and geometric acceptance for Z' to that of the Z contributes uncertainty to the limit. This uncertainty arises from the choice of parton distribution functions, radiative corrections, and statistical precision in the Monte Carlo. The uncertainty is determined in the same manner as for the W' and is found to be 3%.

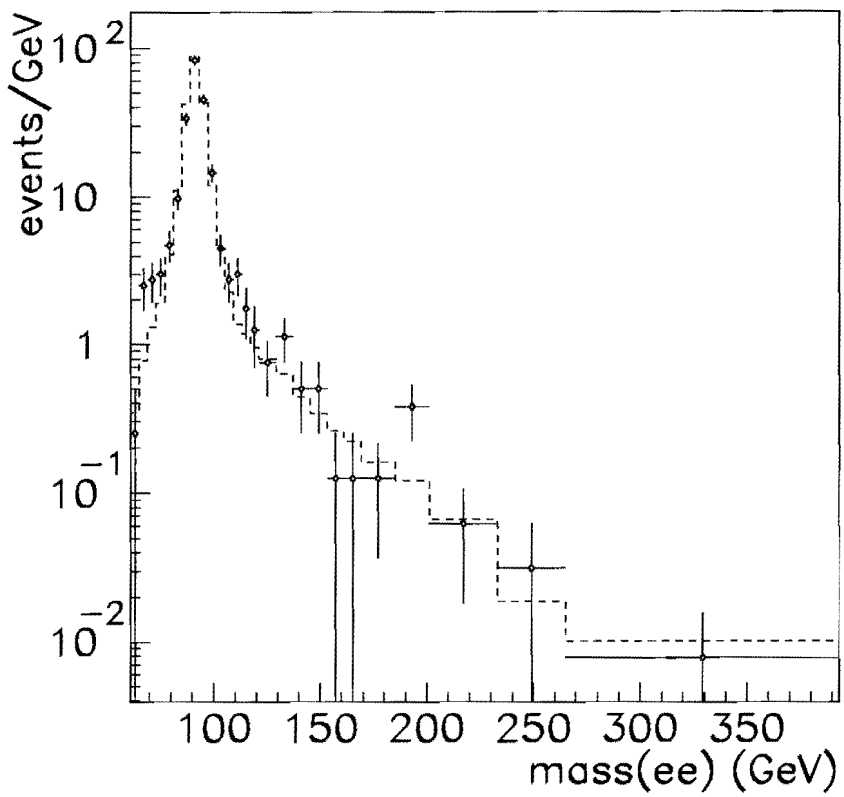

FIG. 4.2: Observed dielectron events (discrete points) are compared to the combined Z–Drell-Yan and QCD background.

4.6 Extracting a limit

A binned likelihood approach with Poisson statistics was applied to the invariant mass distribution in order to obtain an upper limit on the process $p\bar{p} \rightarrow Z' \rightarrow ee$. The procedure is the same as that used for the W' analysis.

The probability that n_i events will be experimentally observed in the ith bin is given by:

$$P_i = \frac{(f_i)^{n_i} e^{-f_i}}{n_i!}$$

where f_i is the number of predicted events. The function f_i is given by:

$$f_i = (1-\alpha) f_i^B + \alpha f_i^{Z'}$$

where f_i^B is the $Z\gamma^*$ plus QCD background, $f_i^{Z'}$ is the Z' signal, and α is a free parameter that is varied from 0 to 1. The functions f_i^B and $f_i^{Z'}$ are each normalized to the number of events in the sample,

$$\sum_i^N f_i^B = \sum_i^N f_i^{Z'} = N_{\text{obs}},$$

where N_{obs} is the number of dielectron events observed experimentally.

The probability density function, $P(\alpha)$, is formed exactly as it was for the W' analysis. The probability density function for the Z' is constructed over the invariant mass region where the expected net Z' signal is positive, $m_{ee} > 0.85 m_{Z'}$. For $m_{Z'} = 100$ GeV, the value is $m_{ee} > 95$ GeV. The binning is chosen so that the number of expected Z' events is approximately equal in each bin. Ten bins were used.

The number of expected Z' events, $N_{Z'}$, is the physical observable that is varied as α is varied. The uncertainty in the scale factor, $A_Z/(A_{Z'} N_Z)$, is transferred to $N_{Z'}$ and included

as an uncertainty in the probability distribution, $P(\alpha)$. This uncertainty consists of the 3% systematic error in $A_{Z'}/A_Z$ and the statistical error on N_Z, 4%. This is combined to give a total error of 5%. There is also uncertainty in $P(\alpha)$ due to the overall normalization of the background in the fit region. The full background sample is normalized to the number of observed events. However only the high invariant mass tail of the background is used in the fit and that region is not independently normalized to the data. That uncertainty arises from the statistical uncertainty in the $Z\gamma^*$ Monte Carlo, the uncertainty in the choice of pdf's, and the uncertainty in the shape and magnitude of the QCD background. The uncertainty in the scaling factor, $A_Z/(A_{Z'}N_Z)$, and the uncertainty in the background are incorporated into the probability density function as Gaussian distributed error. As before, this procedure determines the 95% confidence level limit for $N_{Z'}$,

$$N_{95}^{Z'} = \alpha_{95} \times N_{\text{obs}},$$

where $N_{95}^{Z'}$ is the 95% CL limit on expected Z' events.

The limit $N_{95}^{Z'}$ is expressed as a 95% CL limit on $\sigma B(Z' \to ee)/\sigma B(Z \to ee)$ using

$$\left(\frac{\sigma B_{Z'}}{\sigma B_Z}\right)_{95} = \frac{A_Z}{A_{Z'}N_Z} N_{95}^{Z'}.$$

$A_{Z'}$ is given by:

$$A_{Z'} = \frac{\sigma B_{Z'Z_{\gamma^*}} A_{Z'Z_{\gamma^*}} - \sigma B_{Z_{\gamma^*}} A_{Z_{\gamma^*}}}{\sigma B_{Z'}}$$

where the acceptances are for the invariant mass region of expected Z' signal. A_Z/N_Z is given by:

$$\frac{A_Z}{N_Z} = \frac{\sigma B_{Z_{\gamma^*}} A_{Z_{\gamma^*}}}{\sigma B_Z N_{Z_{\gamma^*}}},$$

where $N_{Z_{\gamma^*}}$ is equal to N_{obs} less QCD background. The acceptances in this case are for the full invariant mass spectrum. It is interesting to note that in the expressions $\sigma B_{Z'Z_{\gamma^*}} A_{Z'Z_{\gamma^*}}$

$m_{Z'}$ (GeV)	m_{ee} min., fit region	observed events	expected background	95% CL, $N_{95}^{Z'}$	95% CL, $\sigma B_{Z'}/\sigma B_Z$ ($\times 10^{-3}$)
100	95	226	190.9 ± 5.5	37.44	41.11
200	140	12	8.3 ± 0.4	9.19	6.45
300	255	1	1.4 ± 0.1	3.84	2.64
400	340	0	0.3 ± 0.1	3.02	2.11
500	425	0	0.1 ± 0.1	3.02	2.16
600	510	0	< 0.1	3.02	2.26

TABLE 4.1: For each Z' mass: minimum m_{ee} of the fit region, the 95% CL expressed as expected events, and the 95% CL expressed as $\sigma B(Z' \to ee)/\sigma B(Z \to ee)$.

and $\sigma B_{Z\gamma^*} A_{Z\gamma^*}$, $\sigma B_{Z'Z\gamma^*}$ and $\sigma B_{Z\gamma^*}$ are not known independently since the cross section for γ^* must have a lower invariant mass bound to remain finite. Table 4.1 gives the 95% CL limit on this ratio, the limit expressed as expected events, the observed events, and the range of the fit for the different Z' masses considered.

The 95% CL limit on the ratio $\sigma B(Z' \to ee)/\sigma B(Z \to ee)$ is plotted as a function of the Z' mass in Fig. 4.3 together with the value of this ratio assuming standard model couplings. The theoretical cross section ratio was determined using Born level cross sections and second order K factors with the MRS D$-'$ pdf set. Again the pdf sets MRS D0$'$ and CTEQ 2M were used to evaluate the uncertainty in that choice. The uncertainty was found to be 3%. As determined by the intersection of the two curves, a Z' with the same couplings to quarks and leptons as the standard model Z is excluded at the 95% CL for $m_{Z'} < 490$ GeV.

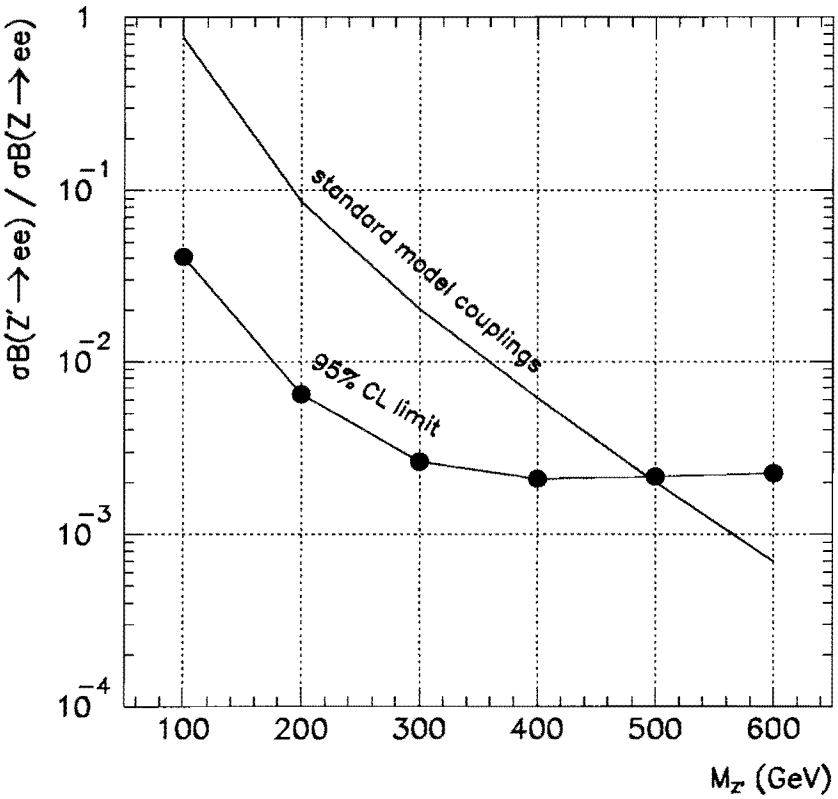

FIG. 4.3: 95% CL upper limit as a function of $m_{Z'}$ for $\sigma B(Z' \to ee)/\sigma B(Z \to ee)$. The expected value using standard model coupling is also shown.

Chapter 5

Conclusions

We have searched for evidence of $W' \to e\nu$ and $Z' \to ee$. Assuming that the neutrino from W' decay is stable and has a mass significantly less than $m_{W'}$, we set an upper limit at the 95% confidence level on the ratio $\sigma B(W' \to e\nu)/\sigma B(W \to e\nu)$ of $\approx 3 \times 10^{-4}$, valid in the range of the search except at low $m_{W'}$ for any W' model. We also set an upper limit on the ratio $\sigma B(Z' \to ee)/\sigma B(Z \to ee)$ of $\approx 3 \times 10^{-3}$, valid for any Z' model in the range of the search except at low $m_{Z'}$. Assuming a particular model for the W' and for the Z' with the same couplings to quarks and leptons as the standard model W and Z, we exclude the existence of a W' of mass less than 610 GeV and a Z' of mass less than 490 GeV at the 95% confidence level. For any realistic Z' model and many W' models, the mass limits would be considerably less.

References

[1] P. Wheelwright, *The Presocratics*, Odyssey Press, New York, 1966,

[2] A.R. Hall and M.B. Hall, *A Brief History of Science*, New American Library, New York, 1964.

[3] A. Pais, *Inward Bound*, Oxford University Press, New York, 1986.

[4] DØ Collaboration, S. Abachi *et al.*, FERMILAB Pub-95/028-E, submitted to Phys. Rev. Lett. CDF Collaboration, F. Abe *et al.*, FERMILAB Pub-95/022-E, submitted to Phys. Rev. Lett.

[5] R.N. Mohapatra, *Unification and Supersymmetry*, Springer-Verlag, New York, 1992.

[6] T. Rizzo, Phys. Rev. D **50**, 325 (1994).

[7] P. Langacker and M. Luo, Phys. Rev. D **45**, 278 (1991).

[8] J. Hewett and T. Rizzo, Phys. Rep. **183**, 193 (1989).

[9] E. Ma, Phys. Rev. D **36**, 274 (1987); Mod. Phys. Lett. A **3**, 319 (1988).

[10] P. Langacker and S.U. Sankar, Phys. Rev. D **40**, 1569 (1989).

[11] J.L. Hewett, T.G. Rizzo, U. of Wisconsin, Madison Pub., MAD-PH-645 (1991).

[12] A.E. Jodidio *et al.*, Phys. Rev. D **34**, 1967 (1986); **37**, 237(E) (1988)); P. Herczeg, Phys. Rev. D **34**, 3449 (1986); J. Imazato *et al.*, Phys. Rev. Lett. **69**, 877 (1992).

[13] G. Beall, M. Bander and A. Soni, Phys. Rev. Lett. **48**, 848 (1982); G. Ecker and W. Grimus, Nucl. Phys. **B258**, 328 (1985).

[14] G. Altarelli and P.J. Franzini, Z. Phys. C **37**, 271 (1988).

[15] F.J. Gilman and M.H. Reno, Phys. Rev. D **29**, 937 (1984).

[16] K.A. Olive, D. Schramm, and G. Steigman, Nucl. Phys. **B180**, 497 (1981).

[17] G. Raffelt and D. Seckel, Phys. Rev. Lett. **60**, 1793 (1988); R. Barbieri and R.N. Mohapatra, Phys. Rev. D **39**, 1229 (1989).

[18] A.S. Carnoy *et al.*, J.Phys. G: Nucl. Part. Phys. **18**, 823 (1992).

[19] CDF Collaboration, F. Abe *et al.*, FERMILAB-Pub-94/268-E, submitted to Phys. Rev. Lett.; UA1 Collaboration, C. Albajar *et al.*, Z. Phys. C **44**, 15 (1989); UA2 Collaboration, R. Ansari *et al.*, Phys. Lett. **B195**, 613 (1987).

[20] CDF Collaboration, F. Abe *et al.*, FERMILAB Pub-94/198-E, submitted to Phys. Rev. Lett.

[21] J. Thompson, FERMILAB-TM-1909, (1994).

[22] DØ Collaboration, S. Abachi *et al.*, Nucl. Instr. Meth. **A338**, 185 (1994).

[23] DØ Collaboration, "Search for the top quark", in preparation.

[24] T. Sjöstrand, Computer Physics Commun. **82**, 74 (1994).

[25] A.D. Martin, R.G. Roberts and W.J. Stirling, Phys. Lett **B306**, 145 (1993); *Erratum* Phys. Lett. **B309**, 492 (1993).

[26] CDF Collaboration, F. Abe *et al.*, FERMILAB-Pub-94/313-E, submitted to Phys. Rev. Lett.

[27] J. Botts, J.G. Morfin, J.F. Owens, J. Qiu, W-K. Tung and H. Weerts, Phys. Lett. **B304**, 159 (1993).

[28] H. Aihara, private communication.

[29] The fast Monte Carlo was provided by P. Yepes, with a few subroutines from J. Sculli.

[30] Q. Zhu, PhD Thesis, New York University, (1994).

[31] U. Heinz and M. Narain, DØ note 1814 (1993).

[32] M. Narain and S. Chopra, DØ note 2105 (1994).

[33] DØ Collaboration, "W and Z Boson Production", in preparation.

[34] CDF Collaboration, FERMILAB Conf-94/155-E.

[35] B. Choudhary, private communication.

[36] W.T. Giele, E.W.N. Glover and D.A. Kosower, Nucl. Phys. **B404**, 633 (1993).

[37] R. Hamberg, W.L. van Neerven, and T. Matsuura, Nucl. Phys. **B359**, 343 (1991).

[38] G. Eppley and H.E. Miettinen, SDC Collaboration, SDC 90-00125 (1990).